



# Eta Carinae: An Evolving View of the Central Binary, Its Interacting Winds and Its Foreground Ejecta

Theodore R. Gull<sup>1,2</sup> , D. John Hillier<sup>3</sup> , Henrik Hartman<sup>4</sup> , Michael F. Corcoran<sup>5,6</sup> , Augusto Damineli<sup>7</sup> , David Espinoza-Galeas<sup>6,8</sup> , Kenji Hamaguchi<sup>5,9</sup> , Felipe Navarete<sup>10</sup> , Krister Nielsen<sup>6</sup> , Thomas Madura<sup>11</sup> , Anthony F. J. Moffat<sup>12</sup> , Patrick Morris<sup>13</sup> , Noel D. Richardson<sup>14</sup> , Christopher M. P. Russell<sup>15</sup> , Ian R. Stevens<sup>16</sup> , and Gerd Weigelt<sup>17</sup>

<sup>1</sup> Exoplanets & Stellar Astrophysics Laboratory, NASA/Goddard Space Flight Center, Greenbelt, MD 20771, USA; [tedgull@gmail.com](mailto:tedgull@gmail.com)

<sup>2</sup> Space Telescope Science Institute, 3700 San Martin Drive, Baltimore, MD 21218, USA

<sup>3</sup> Department of Physics & Astronomy & Pittsburgh Particle Physics, Astrophysics, & Cosmology Center (PITT PACC), University of Pittsburgh, 3941 O'Hara Street, Pittsburgh, PA 15260, USA

<sup>4</sup> Materials Science & Applied Mathematics, Malmö University, SE-20506 Malmö, Sweden

<sup>5</sup> CRESST & X-ray Astrophysics Laboratory, NASA/Goddard Space Flight Center, Greenbelt, MD 20771, USA

<sup>6</sup> The Catholic University of America, 620 Michigan Ave., N.E. Washington, DC 20064, USA

<sup>7</sup> Instituto de Astronomia, Geofísica e Ciências Atmosféricas, Universidade de São Paulo, Rua do Matão 1226, Cidade Universitária São Paulo-SP, 05508-090, Brasil

<sup>8</sup> Departamento de Astronomía y Astrofísica, Facultad de Ciencias Espaciales, Universidad Nacional Autónoma de Honduras, Bulevar Suyapa, Tegucigalpa, M.D.C., Honduras, Centroamérica

<sup>9</sup> Department of Physics, University of Maryland Baltimore County, 1000 Hilltop Circle, Baltimore, MD 21250, USA

<sup>10</sup> SOAR Telescope/NSF's NOIRLab, Avda Juan Cisternas 1500, 1700000, La Serena, Chile

<sup>11</sup> Department of Physics & Astronomy, San Jose State University, One Washington Square, San Jose, CA 95192, USA

<sup>12</sup> Dépt. de physique, Univ. de Montréal, C.P. 6128, Succ. C-V, Montréal, QC H3C 3J7, Canada & Centre de Recherche en Astrophysique du Québec, Canada

<sup>13</sup> California Institute of Technology, IPAC, M/C 100-22, Pasadena, CA 91125, USA

<sup>14</sup> Department of Physics & Astronomy, Embry-Riddle Aeronautical University, 3700 Willow Creek Rd, Prescott, AZ 86301, USA

<sup>15</sup> Department of Physics and Astronomy, Bartol Research Institute, University of Delaware, Newark, DE 19716, USA

<sup>16</sup> School of Physics & Astronomy, University of Birmingham, Birmingham B15 2TT, UK

<sup>17</sup> Max Planck Institute for Radio Astronomy, Auf dem Hügel 69, 53121 Bonn, Germany

Received 2022 April 14; revised 2022 May 16; accepted 2022 May 29; published 2022 July 13

## Abstract

FUV spectra of  $\eta$  Car, recorded across two decades with HST/STIS, document multiple changes in resonant lines caused by dissipating extinction in our line of sight. The FUV flux has increased nearly tenfold, which has led to increased ionization of the multiple shells within the Homunculus and photodestruction of H<sub>2</sub>. Comparison of observed resonant line profiles with CMFGEN model profiles allows separation of wind–wind collision and shell absorptions from the primary wind P Cygni profiles. The dissipating occulter preferentially obscured the central binary and interacting winds relative to the very extended primary wind. We are now able to monitor changes in the colliding winds with orbital phase. High-velocity transient absorptions occurred across the most recent periastron passage, indicating acceleration of the primary wind by the secondary wind, which leads to a downstream, high-velocity bow shock that is newly generated every orbital period. There is no evidence of changes in the properties of the binary winds.

*Unified Astronomy Thesaurus concepts:* Massive stars (732); Stellar winds (1636)

## 1. Introduction

Eta Carinae ( $\eta$  Car) is the most luminous, most massive star within 3 kpc. In the 1840s, it underwent a massive explosion, ejecting a nebula now known as the Homunculus, which has expansion velocities of  $\sim 650 \text{ km s}^{-1}$  (Hillier & Allen 1992; Steffen et al. 2014). The mass of the nebula is believed to range from 10 to greater than  $45 M_{\odot}$  (Morris et al. 2017). An additional, less energetic eruption occurred in the 1890s (Smith & Frew 2011). Possible earlier eruptions have been suggested by Kiminki et al. (2016). These events, and possibly others, have given rise to a very complex circumstellar environment that is associated with  $\eta$  Car.

$\eta$  Car provides an important, nearby example of those rare binary stars that inhabit the upper region of the Hertzsprung–Russell diagram, and which are responsible for extreme

supernovae, gamma-ray bursts and black holes near the upper boundary of the lower black hole mass gap (The LIGO Scientific Collaboration et al. 2021). Despite more than two centuries of dedicated study,  $\eta$  Car's evolutionary path and its current evolutionary state are not constrained. Periodic spectral (Damineli 1996; Damineli et al. 1997) and X-ray emission variations (Ishibashi et al. 1999; Corcoran 2005) show that  $\eta$  Car is a long-period, highly eccentric, colliding-wind binary system consisting of a near 100 solar mass primary,  $\eta$  Car-A, and a smaller, massive star companion,  $\eta$  Car-B. We do not know whether the presence of the companion star is fundamental to the current state of the primary (through mass and/or angular momentum exchange, for example), or incidental to it. It is very difficult to constrain the stellar parameters of the companion, because it is lost in the glare of the primary star at nearly all wavelengths.

The clearest evidence we have of the companion is from the X-rays produced when the companion's wind, deduced to be moving near  $3000 \text{ km s}^{-1}$  based on analysis of X-ray spectra (Pittard & Corcoran 2002), collides with the dense, slow-moving



Original content from this work may be used under the terms of the [Creative Commons Attribution 4.0 licence](https://creativecommons.org/licenses/by/4.0/). Any further distribution of this work must maintain attribution to the author(s) and the title of the work, journal citation and DOI.

wind ( $420 \text{ km s}^{-1}$ ; Groh et al. (2012b)) of the primary star. Indirect evidence comes from transient high-velocity absorptions (Groh et al. 2010; Richardson et al. 2016; Gull et al. 2021) extending to speeds of  $900$  to  $2200 \text{ km s}^{-1}$  (two to five times the terminal speed of the primary wind), presumably arising from the primary wind being accelerated by the faster wind of the secondary. Variable ionization of the circumstellar ejecta due to a combination of the UV radiation from the companion star and from the primary star (which leaks through the colliding wind shock cone that surrounds the secondary, periodically illuminating different circumstellar structures like a searchlight) also provides important information about the temperature and luminosity of the companion star. Analysis of the changing circumnebular ionization across periastron passages and over longer timescales indirectly suggests that the companion is a hot star, about a third as massive as  $\eta$  Car-A and probably about one-fifth as luminous (Verner et al. 2005; Mehner et al. 2010), similar to other extreme stars in the Carina Nebula.

Our view of the central binary has been obscured by the presence of an optically thick “occultor” (Hillier & Allen 1992; Weigelt et al. 1995; Falcke et al. 1996; Hillier et al. 2001, 2006) close to the star and in our line of sight (LOS). Evidence shows that this occultor has now dissipated to such an extent that  $\eta$  Car is once again near naked-eye visibility for the first time since before the Great Eruption (when it was near a visual magnitude of  $\approx 3.5$ ) (Damineli et al. 2019, 2021). The decline in this occultor provides us a much-improved view of the FUV (1150 to  $1680 \text{ \AA}$ ) emission from the inner binary. Absorptions at velocities near  $-513 \text{ km s}^{-1}$  arise from the 1840s eruption that produced the Homunculus, while slower absorptions near  $-146 \text{ km s}^{-1}$  arise from the 1890s event. Many weaker absorptions at velocities ranging from  $-121$  to  $-1000 \text{ km s}^{-1}$  are also detectable (Gull et al. 2006). Seeing-limited spectra include emission-line contributions from the Weigelt clumps (Weigelt & Ebersberger 1986) and fainter structures at  $-40 \text{ km s}^{-1}$  (Gull et al. 2016).

In this paper, we examine changes in FUV spectra of  $\eta$  Car, recorded over the past 20 years with the Hubble Space Telescope/ Space Telescope Imaging Spectrograph (HST/STIS).<sup>18</sup> We consider spectra taken at intervals across nearly four orbital cycles, with many recorded at nearly the same orbital phase, as is necessary to disentangle non-phase-related (secular) variations from phase-dependent ones.

The primary objectives of our work are to search for direct evidence of the companion star and its wind, to search for signatures of wind–wind interaction, and to quantify and understand the changes in the spectrum as a function of orbital phase and over time. Of particular interest is discerning whether changes in the spectrum over the last two decades, sampling three binary orbits, require changes in the primary star, or whether they can be explained solely by variations in the circumstellar medium around  $\eta$  Car.

This paper is organized as follows:

1. Section 2 describes the various structures known to lie in our LOS, as well as potential contributions to the resonant line absorptions.

2. Section 3 catalogs the observations discussed herein.
3. Section 4 presents profiles of resonant lines of interest broken down into these subsections:
  - (a) wind lines of interest (4.1);
  - (b) a description of the CMFGEN model used to help disentangle “classical” wind features (4.2);
  - (c) Ni II  $\lambda 1455$  observed versus CMFGEN (4.3);
  - (d) Ni II  $\lambda 1455$  changes across periastrons 11 and 14 (4.4).
4. Section 5 describes profiles at similar binary phases:
  - (a) profiles at nearly the same phase of three binary periods (5.1);
  - (b) observed profiles of doublet members (5.2);
  - (c) observed profiles compared to CMFGEN profiles (5.3);
  - (d) long-term profile changes between periastron passages 11 and 14 (5.4);
  - (e) profile changes across periastron passages 11 and 14 (5.5).
5. Section 6 discusses these results.
6. Section 7 summarizes our conclusions and suggests future observations.

## 2. Setting the Stage

The structures of  $\eta$  Car and its circumstellar ejecta are far from simple. Three-dimensional hydrodynamical (3D hydro) models of the interacting winds, compared to maps of spatially resolved, visible-wavelength forbidden emission lines, suggest that the binary orbital pole is closely aligned with the axis of symmetry of the bipolar Homunculus (Gull et al. 2009; Madura et al. 2012; Gull et al. 2016). Our LOS intersects the orbital plane tilted  $49^\circ$  out of the sky plane. The orientations of the stars around their orbits result in circumnebular ionization variations with binary orbital phase. These changes are especially apparent across periastron passage, due to the rapidly changing orientations of the two stars and consequent changes in the interacting winds. Longer-term changes in the circumnebular environment, as well as sporadic changes to the stars themselves, can result in non-phase-dependent variations in the spectrum as well. As a result, changes in narrow line absorptions associated with two large ejection events are seen near periastron passage and over the long term. To aid our discussion, Figure 1 shows a simple sketch that defines the structures near periastron and apastron along our LOS from the binary through its interacting winds and circumstellar absorption shells. Figure 2 displays expected absorption signatures of these structures sketched in Figure 1.

The periastron event occurs with  $\eta$  Car-B buried deeply within the primary wind on the far side of  $\eta$  Car-A. This leads to the observed low-ionization states of  $\eta$  Car-A and of the distant foreground shells within the Homunculus every periastron passage.  $\eta$  Car-B is immersed in the primary wind for several weeks while the primary wind flows unimpeded in our direction.  $\eta$  Car-B then emerges from the primary wind, and the secondary wind creates a chaotic acceleration of primary wind in our direction (Gull et al. 2021) and rebuilds the ionization cavity, which is bounded by the swept-up primary wind. The very fast wind of  $\eta$  Car-B creates a rapidly expanding, highly ionized, low-density cavity, and in diluted form, accelerates and compresses the swept-up primary wind along the downstream walls of the bow shock. Our LOS from

<sup>18</sup> Based on observations made with the NASA/ESA Hubble Space Telescope, obtained at the Space Telescope Science Institute, which is operated by the Association of Universities for Research in Astronomy, Inc., under NASA contract NAS5-26555. The new observations were part of Chandra program 20200564 and are associated with HST programs 15611 and 15992.

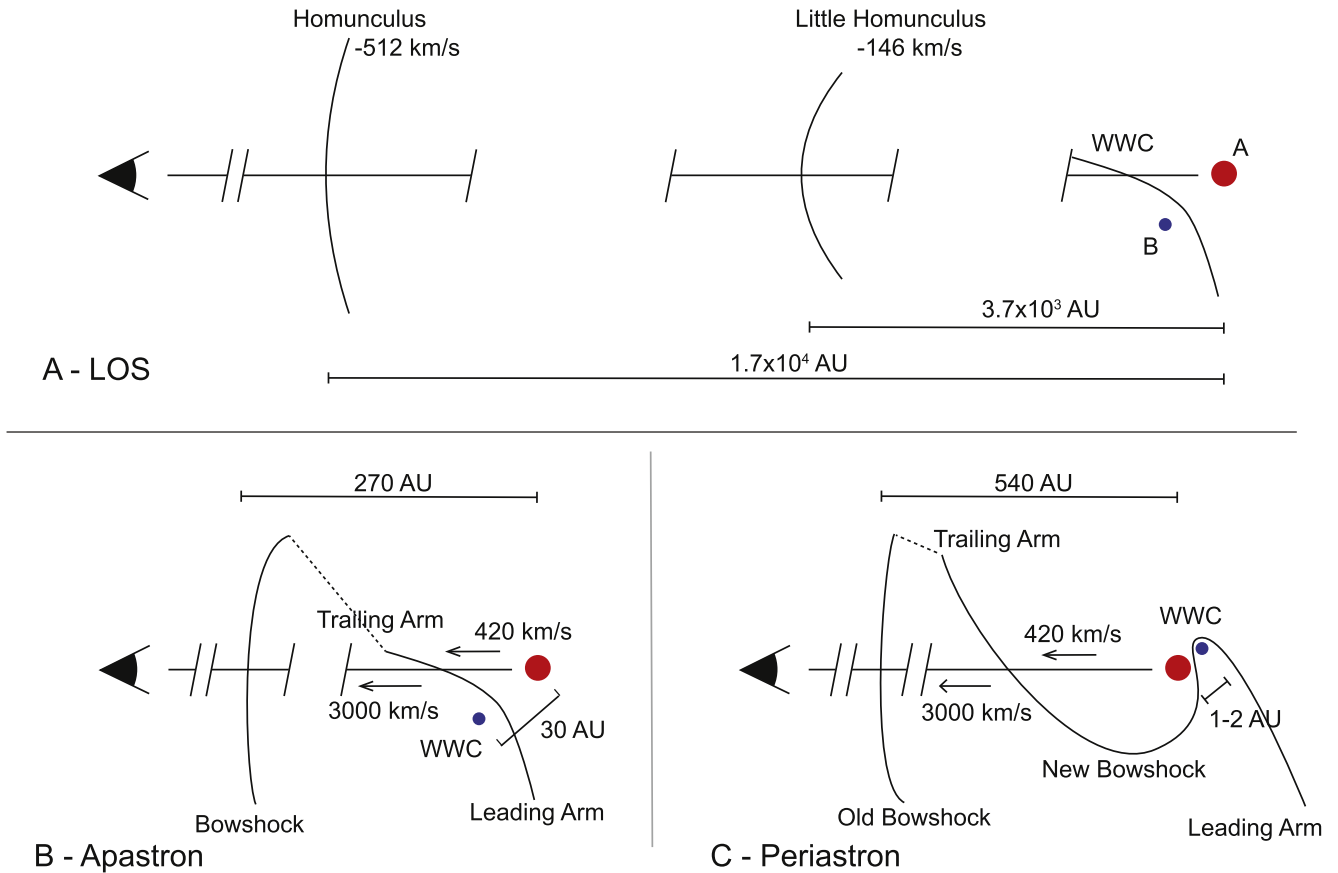


**Figure 1.** Sketches defining the structures in our LOS from  $\eta$  Car. Panel A: Large-scale structure in LOS at apastron. The binary companions are separated by  $\approx 30$  au, with  $\eta$  Car-B on the near side of  $\eta$  Car-A. Our LOS of  $\eta$  Car-A, the principal source of radiation longward of  $\text{Ly}\alpha$ ,  $1216 \text{ \AA}$ , passes through the highly shocked, wind-wind collision (WWC) zone close to the leading edge of the cavity carved by the wind of  $\eta$  Car-B out of the wind of  $\eta$  Car-A for most of the orbit. In our LOS, we observe two series of shells, the first characterized by the  $-146 \text{ km s}^{-1}$  Little Homunculus,  $3700 \text{ au}$  from  $\eta$  Car, and the second characterized by the  $-512 \text{ km s}^{-1}$  Homunculus,  $170,000 \text{ au}$  from  $\eta$  Car. Panel B: Enlargement of the interacting binary at apastron. The stronger WWC zone, the X-ray source, is located between the two stars, separated by  $30 \text{ au}$ . A secondary structure, the bow shock, exists at a distance of  $270 \text{ au}$ , being the result of the secondary wind blowing a cavity out of the primary wind. Panel C: Enlargement of the interacting binary near periastron. The WWC zone wraps around  $\eta$  Car-A as  $\eta$  Car-B passes to the far side. At a distance of  $540 \text{ au}$ , the bow shock continues to expand at  $\approx 500 \text{ km s}^{-1}$  in our LOS. For a brief interval at the beginning of the periastron passage, the trailing arm passes in front of  $\eta$  Car-A, leading to a newly created cavity and bow shock in our LOS. Note that our LOS is at  $49^\circ$  to the binary orbital plane.

the FUV source,  $\eta$  Car-A, views the interior of the ionized cavity around  $\eta$  Car-B and the bow shock formed by the primary wind after each periastron passage. Both the cavity and the bow shock continuously expand for most of the 5.54-year orbit, only to be replaced by a new cavity bounded by a new bow shock; in other words, a train of low-density cavities bounded by bow-shock walls accumulates and extends across our LOS.

The core of  $\eta$  Car-A is the primary continuum source longward of  $\text{H I Ly}\alpha$ , consistent with both observations and CMFGEN models (Hillier et al. 2006). However the hotter, less luminous  $\eta$  Car-B increasingly contributes flux at shorter wavelengths in the FUV and dominates below  $\text{H I Ly}\alpha$  ( $< 912 \text{ \AA}$ , the EUV) (Iping et al. 2005). As each periastron passage occurs, the ionization and the excitation of the Weigelt clumps fall as they are cut off from  $\eta$  Car-B's ionizing radiation by the inner wind of  $\eta$  Car-A (Zethson et al. 2001; Hartman et al. 2005; Verner et al. 2005; Zethson et al. 2012). A drop in ionization can also be seen in the circumstellar gas along our LOS, producing the various absorption components (Gull et al. 2006).

The continuum-emitting primary-wind core, with a diameter of  $6.5 \text{ au}$  in mid-IR Very Large Telescope Interferometer (VLTI) images taken near periastron, extends beyond the  $1$  to

$2 \text{ au}$  separation of the binary (Weigelt et al. 2021). Mid-IR measurement resolved the  $\text{H I Br}\alpha$ , which demonstrated that the low-ionized portion of the primary wind extends to at least  $60 \text{ au}$  (Weigelt et al. 2021), well beyond the major axis of the binary orbit ( $\approx 28 \text{ au}$ ).

We identify absorption signatures of specific structures in our LOS as follow:

1. The extended, cooler primary wind provides a PCygni profile with  $V_{\infty, A} = 420 \text{ km s}^{-1}$  (Figure 2, Top). CMFGEN modeling suggests PCygni profiles are present in the low-ionization resonant lines (Section 4.2). Two example profiles are  $\text{Ni II}$  and  $\text{Si II}$ .  $\text{C II}$ ,  $\text{Al II}$ ,  $\text{Al III}$ , and possibly  $\text{Si IV}$  also show evidence of PCygni wind profiles (Figures 3, 8, and 9).
2. The evolving bow shock provides absorption in our LOS (Figure 2, Middle): Following the 3D hydro modeling of Madura (2010) and Madura et al. (2012), the WWC exists in two spatially separate regions:
  - (a) The highly shocked secondary gas between the binary stars gives rise to X-rays (Corcoran et al. 2017). Across the high-ionization state, the leading arm of the shock is located in front of  $\eta$  Car-A. The secondary wind inhibits the flow of the primary wind in our

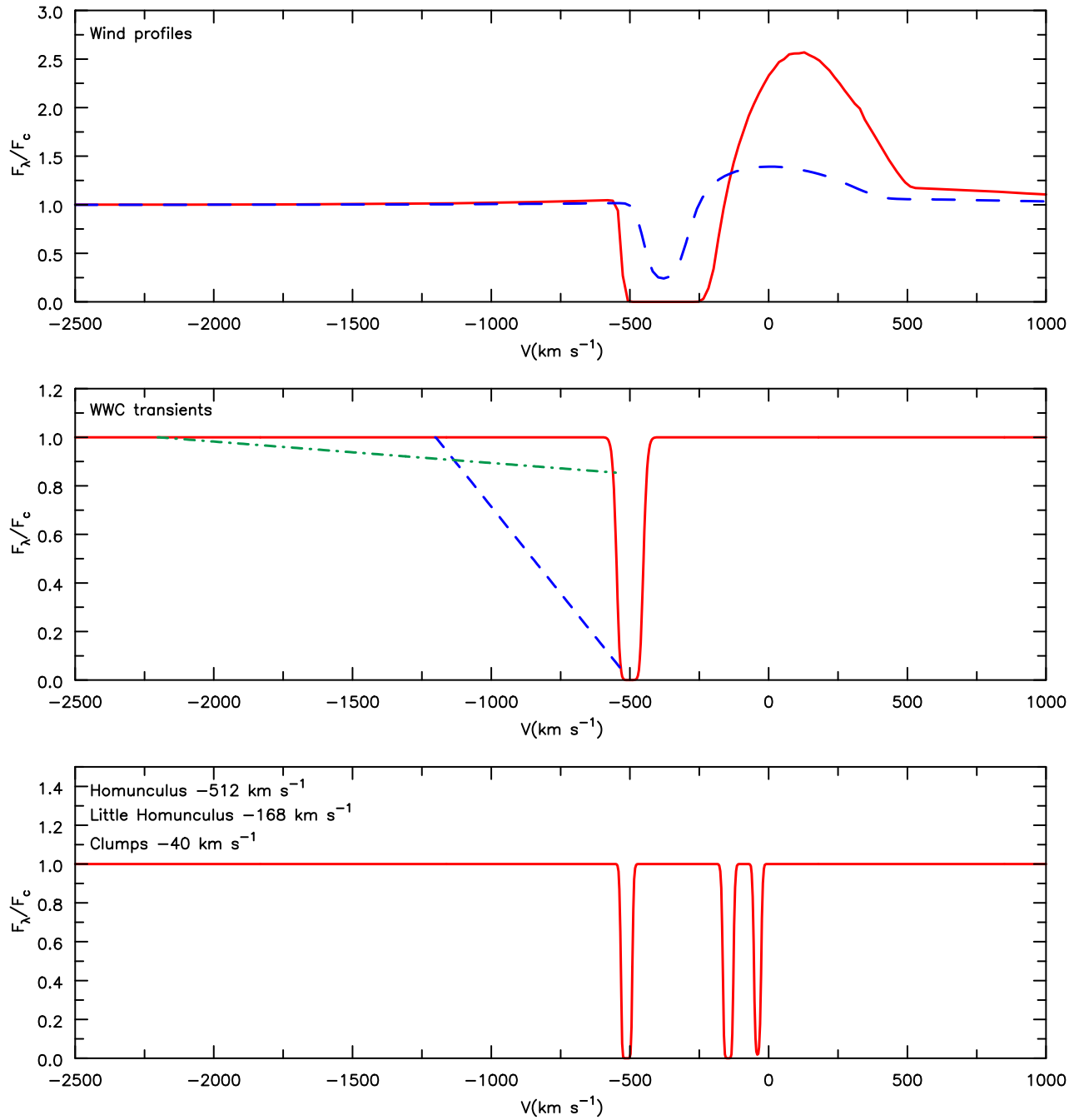


**Figure 2.** Absorption signatures of structures as sketched in Figure 1 in our LOS. Top: CMFGEN model calculations predict saturated P Cygni profiles (red) and unsaturated profiles (blue) in transitions belonging to lower-ionization species such as Si II and Ni II, but not in high-ionization lines such as N V or C IV. Middle: Representation of the variable WWC transient absorptions that have been observed in He I  $\lambda 10830$  extending to  $-2200 \text{ km s}^{-1}$  by Groh et al. (2010) (green) and in FUV Si II resonant lines exceeding  $-1200 \text{ km s}^{-1}$  across the 2020 periastron passage by Gull et al. (2021) (Blue). Variable absorption from a portion of  $\eta$  Car-A's wind could also appear in high-ionization resonant lines (C IV, N V) accelerated by the wind of  $\eta$  Car-B and highly ionized by the flux of  $\eta$  Car-B (red). Bottom: Thirty-six narrow ( $\approx 5.5 \text{ km s}^{-1}$  FWHM) absorption velocities from shells were identified by Gull et al. (2006). The strongest absorptions, schematically shown, are at velocities  $-512 \text{ km s}^{-1}$  (Homunculus),  $-146 \text{ km s}^{-1}$  (Little Homunculus) and  $-40 \text{ km s}^{-1}$  (Weigelt clumps located very near  $\eta$  Car). With the tenfold increase of FUV flux over the past two decades, many metals in these shells have increased from singly ionized states to multiply ionized states, and the  $\text{H}_2$  in the Homunculus has been destroyed in our LOS.

direction but provides little absorption, while its EUV radiation leads to higher ionization of the primary wind. Little absorption is expected in the FUV during the high-ionization state from the shock boundary.

- (b) As the binary system approaches periastron passage,  $\eta$  Car-B plunges deep into the primary wind. The trailing arm of the WWC wraps around  $\eta$  Car-A, leading to ionization and acceleration of the distorted primary

wind. Both Groh et al. (2010) and Richardson et al. (2016) saw evidence of this trailing arm before periastron passages in cycles 12 and 13 in the form of high-velocity absorption of He I lines in the visible and the near red. Groh et al. (2010) also reported the presence of the trailing arm in FUV resonant lines as the binary approached periastron passage 11. In the FUV, multiple resonant lines show a transient absorption wing



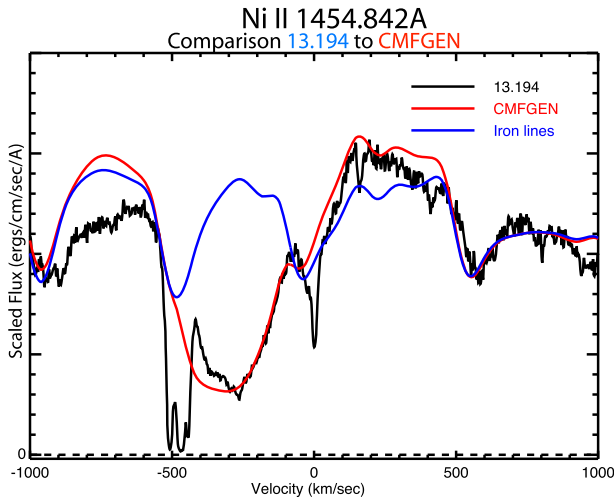


**Figure 3.** Ni II  $\lambda 1455$  velocity plot from  $\phi = 13.194$  compared to a CMFGEN-generated model of  $\eta$  Car-A and the same model but showing only line contributions by iron. The CMFGEN-generated model reproduces the UV spectrum of  $\eta$  Car remarkably well. Most of the UV portion of the  $\eta$  Car spectrum is heavily modulated by low-ionization iron lines, as notable here. The CMFGEN velocity profile, generated for  $V_\infty = 420 \text{ km s}^{-1}$  (Groh et al. 2012a), closely follows the Ni II  $\lambda 1455$  velocity profile quite well. Exceptions are caused by two velocity systems originating from ejecta: narrow Ni II  $\lambda 1455$  centered at  $+4 \text{ km s}^{-1}$  blended with an iron absorption to the blue and a complex of absorptions above and below the  $-513 \text{ km s}^{-1}$  velocity of the Homunculus (Gull et al. 2006).

that is saturated at  $-500 \text{ km s}^{-1}$  and extends to  $-1000$  to  $-1500 \text{ km s}^{-1}$  (Figure 2, middle).

- (c) For several weeks or more when the secondary is near superior conjunction, the primary wind flows unimpeded in our LOS. As  $\eta$  Car-B moves from behind  $\eta$  Car-A, a new wind cavity becomes visible and the leading arm again passes in front of  $\eta$  Car-A. A bow shock then forms out of the downstream primary wind that is moderately accelerated by the secondary wind and more highly ionized by  $\eta$  Car-B's EUV radiation. The apparent net result is absorption from the accelerated wind of  $\eta$  Car-A over multiple ionization states extending from velocities of  $-400$  to  $-600 \text{ km s}^{-1}$  (Figure 2, middle).

Near periastron passage, the dense walls of the WWC are expected to contribute transient FUV absorptions extending to high velocities (as seen, for example, in the visible and near-IR He I lines by Groh et al. (2010) and Richardson et al. (2016), and in the FUV Si II resonant lines by Gull et al. (2021)), along with absorptions that persist for much of the orbit.

1. Narrow-line absorption at three dozen discrete velocities ranging from  $-122$  to  $-1074 \text{ km s}^{-1}$  were identified by Gull et al. (2006) (Figure 2, bottom). Some were at velocities near characteristic absorption velocities associated with the Little Homunculus ( $-146 \text{ km s}^{-1}$ ) or the Homunculus ( $-512 \text{ km s}^{-1}$ ), but some were at even higher blueshifted velocities.

The dissipation of the occulter, located within the Little Homunculus (Figure 1), causes systematic, long-term changes in the observed stellar spectrum. Because it preferentially blocked the central stars and the WWC region more so than the extended primary wind, the dissipation of the occulter has led to changes in the spectrum, even if the stellar fluxes are constant. In the visible, the dissipation of the occulter has led to a decline in the

**Table 1**  
Log of HST/STIS Observations<sup>a</sup>

Date	Phase <sup>b</sup>	Aperture <sup>c</sup>	Gratings
2002-01-20	10.736	$0''.3 \times 0''.2$	E140M, E230M
2002-07-04	10.818	$0''.3 \times 0''.2$	E140M, E230M
2003-02-13	10.928	$0''.3 \times 0''.2$	E140M, E230M
2003-05-26	10.979	$0''.3 \times 0''.2$	E140M, E230M
2003-07-01	10.998	$0''.3 \times 0''.2$	E140M, E230M
2003-07-29	11.010	$0''.2 \times 0''.2$	E140M, E230M
2003-09-21	11.037	$0''.3 \times 0''.2$	E140M, E230M
2004-03-06	11.119	$0''.3 \times 0''.2$	E140M, E230M
2015-09-02	13.194	$0''.2 \times 0''.2$	E140M, E230M
2018-04-21	13.670	$0''.2 \times 0''.2$	E140M, E230M
2019-06-10	13.886	$0''.2 \times 0''.2$	E140H
2019-08-25	13.913	$0''.2 \times 0''.2$	E140H
2019-12-28	13.975	$0''.2 \times 0''.2$	E140H
2020-02-08	13.995	$0''.2 \times 0''.2$	E140H
2020-03-09	14.010	$0''.2 \times 0''.2$	E140H
2020-03-11	14.011	$0''.2 \times 0''.2$	E140M, E230M
2020-04-01	14.022	$0''.2 \times 0''.2$	E140H
2021-01-26	14.170	$0''.2 \times 0''.2$	E140M, E230M

#### Notes.

<sup>a</sup> Additional HST/STIS FUV spectra of  $\eta$  Car were recorded, but we only list those at similar phases along with additional spectra that are key to tracking changes in resonant line profiles relevant to this discussion.

<sup>b</sup> Phase refers to the binary orbital phase based on both disappearance of He I emission and X-ray drop with periastron passage, numbered 13 occurring on JD 2456874.4  $\pm$  1.3 days, and orbital period of 2022.7  $\pm$  0.3 days (Teodoro et al. 2016). The periastron number refers to the convention based upon detected periastron passages via visible spectroscopy beginning February 1948. While there is general agreement on the period, observations and models do not concur on the actual time of the periastron event, which is thought to be several days earlier than this reference date.

<sup>c</sup> Spectra using the unsupported aperture  $0''.3 \times 0''.2$  were extracted with STIS-team software for a stellar source excluding extended wind background. For details, see Gull et al. (2021).

EWs of many H I, Fe II, and [Fe II] emission lines, since the observed continuum has increased. It has also influenced the strength of the P Cygni absorption profiles associated with Si II and N II (Damineli et al. 2021), (Damineli et al. submitted).

### 3. The Observations

A series of HST/STIS high-dispersion FUV spectra were recorded in coordination with Chandra observations following the spectroscopic X-ray changes across  $\eta$  Car's periastron event in 2020.2 (Espinoza Galeas 2021; Espinoza et al., accepted). The dates of observations and relevant binary orbital phases are listed in Table 1. The HST/STIS visits were planned close to the scheduled CHANDRA visits (1) to establish a baseline of spectral changes as the binary approached periastron, and (2) to sample changes across periastron, following the drop to a low-ionization state of the interacting winds and the Homunculus shells when the hot secondary star is embedded deep within the primary wind and the EUV flux of  $\eta$  Car-B is blocked.

A previous series of STIS FUV spectra had been recorded through multiple programs. Many of these spectra, because they were recorded as similar binary orbital phases, lent themselves to direct comparisons (Table 1).

The observed FUV flux of  $\eta$  Car has increased tenfold since 2000 when initial observations were obtained with HST/STIS. Because of the increasing brightness of  $\eta$  Car, the medium-resolution echelle modes (E140M and E230M) previously used to

monitor the spectral changes from 1150 to 2350 Å could not be used for these new observations, as the predicted global count rate approached the safety limits of the Multi-Anode-Microchannel-Array (MAMA) detectors. We therefore switched to the higher-dispersion echelle mode, E140H, which unfortunately limited observations acquired in a single HST orbit visit to three cross-dispersed grating settings. We chose to monitor the most important resonant lines located between 1150 and 1680 Å with three grating settings: 1234, 1416, and 1598 Å. This meant we were unable to monitor other resonant lines of interest, such as the Al III  $\lambda\lambda$  1855,1863 doublet in the mid-ultraviolet spectral region covered by the E230M grating setting.

Where applicable to this study, we included other HST/STIS FUV spectra of  $\eta$  Car from the public MAST archive. We also included archived E230M spectra to examine the profiles of Al III  $\lambda\lambda$  1855,1863. Additional details on the stellar spectral extractions, specifically from the observations that utilized the 0".3 $\times$ 0".2 aperture, are described in Gull et al. (2021).

#### 4. Resonant Lines and What They Tell Us about Structures in the LOS

##### 4.1. Wind Lines of Interest

The FUV interval includes an abundance of resonant lines from neutral as well as singly and multiply ionized elements. Indeed, much of the challenge is sorting out the contributions from various line transitions and identifying the emitting and absorbing structures in the LOS. The lines discussed are given in Table 2 along with the ionization potentials (IP) for selected atomic/ionic species. For most of the transitions, the lowest level of the transition is either the ground term, or a low-lying level that is easily excited. Thus, the relevant IP for observing a particular ionization stage is that belonging to the previous ionization stage. For example, to get the C IV resonance transitions, we generally need photons (or electrons) with energies greater than 64.5 eV (i.e., the IP of C<sup>+</sup>). In the inner wind, where densities are high and the radiation not strongly diluted, slightly lower photon energies may suffice because in some cases the ionization can be maintained via ionizations from excited states (Johansson & Letokhov 2004a). In some cases it is also possible that a species will give rise to a strong UV profile, even though it is never the dominant ionization stage.

$\eta$  Car-A's prominent wind lines are from singly ionized carbon, silicon, aluminum, iron, and nickel, plus doubly ionized aluminum. In the primary wind, the ions giving rise to these lines can all be produced via photoionization from the primary. However, for the outer ejecta (e.g., Weigelt clumps, Little Homunculus) an additional source of radiation is needed. This is particularly true for doubly ionized species and any species with an IP close to that of hydrogen (e.g., neutral carbon). This occurs because hydrogen recombines in the outer wind of the primary without the radiation from the companion star. Narrow emission lines of [Fe III], [Ne III], [S III], and [Ar III] from the Weigelt clumps disappear at periastron when the secondary star goes behind the primary (Johansson & Letokhov 2004b; Damineli et al. 2008; Gull et al. 2009). Absorption lines of C I and N I are also seen in the spectra, especially below 1350 Å, but that portion of the spectrum is so crowded that only very limited intervals in velocity can be studied for some specific resonant lines.

**Table 2**  
Resonant Lines and Element Ionization Potentials<sup>a</sup>

Spectrum	log <i>gf</i>	Excitation energy		Wave-length Å	Velocity <sup>b</sup> range km s <sup>-1</sup>
		Lower eV	Upper eV		
N V	-0.505	0.000	10.008	1238.821	≈2000
N V	-0.807	0.000	9.976	1242.804	915
C IV	-0.419	0.000	8.008	1548.187	≈3000
C IV	-0.720	0.000	7.995	1550.774	498
Si IV	0.011	0.000	8.896	1393.755	≈4000
Si IV	-0.292	0.000	8.896	1402.770	1939
C II	-0.589	0.000	9.290	1334.532	≈4000
C II	-1.293	0.008	9.290	1335.663	
C II	-0.335	0.008	9.290	1335.708	284
Si II	-0.575	0.000	8.121	1526.707	≈4000
Si II	-0.274	0.036	8.121	1533.431	1320
Al II	-0.248	0.000	7.421	1670.842	≈4000
Al III	+0.050	0.000	6.685	1854.716	≈4000
Al III	-0.253	0.000	6.656	1862.789	1305
Ni II <sup>c</sup>	-0.447	0.000	8.450	1454.842	≈3000
Ni II	-1.176	0.000	8.450	1467.259	

Element	Ion charge <sup>a</sup>					
	0 eV	+1 eV	+2 eV	+3 eV	+4 eV	+5 eV
Ne	21.5	41.0	63.4	97.2	126	158
Ar	15.8	27.6	40.7	59.6	75	91
N	14.5	29.6	47.4	77.5	98	552
C	11.3	24.4	47.9	64.5	392	490
Si	8.2	16.4	33.5	45.1	167	205
Fe	7.9	16.2	30.7	54.9	75	99
Ni	7.6	18.2	35.2	59.4	76	108
Al	6.0	18.8	28.5	119.3	154	190

#### Notes.

<sup>a</sup> Lines and ionization potentials from NIST.

<sup>b</sup> Upper value is an estimate of the quasi-clear velocity interval before strong absorption occurs. Lower value is the effective velocity interval between doublet members due to spectral separation. (The Al II line does not have a doublet companion).

<sup>c</sup> From the Atomic spectral line database (Kurucz).

In addition to absorption lines from singly ionized and neutral species, resonance doublets of higher-ionization species, such as Si IV, C IV, and N V, are also seen (Section 4.2). The high-ionization Si IV and C IV P Cygni profiles, and the weaker absorption associated with N V, cannot be produced by photoionization from the primary star. These lines must either be associated with the secondary wind, the wind–wind shocked region, or other outflowing gas bathed in the UV radiation field of the secondary and/or gas illuminated by X-rays arising from the wind–wind shock.

The resonant absorption lines trace the ionization of different structures in our LOS. For example, the C II  $\lambda\lambda$  1335,1336 absorptions occur in gas in the ionization range from 11.3 to 24.4 eV, and likewise the C IV  $\lambda\lambda$  1548,1551 absorptions trace gas at an ionization state above 64.5 eV. N V  $\lambda\lambda$  1239,1242 absorptions originate in gas ionized above 98 eV. Hence, we have a means of estimating the range of ionization for structures in the LOS ranging from 6.0 eV (Al II 6.0 to 18.8 eV) to >98 eV (N V >98 eV), as shown in Table 2.

Most of the lines studied in this paper have nearby companion lines due to transitions to a second upper level or from an energy level close to the ground state. N V, C IV, Si IV,

and Al III have resonances to two different upper levels. Si II and C II have a low-lying energy level that can be thermally populated. Resonant lines are seen in cold, interstellar clouds<sup>19</sup> but the companion line is absent. However, the companion line is present in the hotter wind structures and multiple discrete shells of gas within the Homunculus. Among the resonant lines with well-defined profiles, only the Al II  $\lambda 1671$  line lacks a companion.

Doublet line separations range in velocity from  $280 \text{ km s}^{-1}$  (C II)<sup>20</sup> to  $1320 \text{ km s}^{-1}$  (Si II). Limited strong absorptions from other lines probe relatively clear velocity intervals up to  $4000 \text{ km s}^{-1}$  shortward of the blue doublet line. While the C II doublet separation is insufficient to separate individual line absorption across a  $600 \text{ km s}^{-1}$  range, the C II doublet can be used to track variable high-velocity absorptions extending as negative as  $-1900 \text{ km s}^{-1}$  (Groh et al. 2010). We use these resonant doublets to help understand the influence of line blends, to search for absorptions up to  $-3000 \text{ km s}^{-1}$  (the terminal velocity of the  $\eta$  Car-B's wind), and to study the 0 to  $-600 \text{ km s}^{-1}$  interval, which is strongly affected by broad absorptions ( $\Delta V \approx$  hundreds of  $\text{km s}^{-1}$  in width) from the primary wind, which are much broader in velocity than the circumnebular absorptions ( $\Delta V \approx 5$  to  $10 \text{ km s}^{-1}$ , Gull et al. 2006) and which often have associated emission as well.

#### 4.2. Description of the CMFGEN Model

The adopted model is the same used to interpret Very Large Telescope Interferometer (VLTI) observations by Weigelt et al. (2021). The parameters are similar, but not identical, to those found by Hillier et al. (2001) and Groh et al. (2012a). A slightly larger radius was adopted than in earlier studies to weaken He I lines—these lines are now believed to have a substantial contribution from the bow shock (e.g., Nielsen et al. 2007). Even larger radii can be used to explain the spectroscopic observations, but these are probably ruled out by the high eccentricity of the binary orbit. With  $e = 0.9$  and  $a = 15 \text{ au}$ , the periastron distance of  $1.5 \text{ au}$  is already uncomfortably close to the radius of the primary star ( $0.56 \text{ au}$ ).

In our modeling, we assumed  $d = 2.3 \text{ kpc}$  (Allen & Hillier 1991), which is very similar to the most recent Gaia EDR3 determinations of distance to the star clusters Trumpler 14, 15, and 16 (Shull et al. 2021). In practice, revised stellar parameters for a new distance can be obtained through a simple scaling ( $L \propto d^2$ ,  $R \propto d^2$ ,  $\dot{M} \propto R^{3/2}$ ). A detailed discussion of the complex issues surrounding the modeling of the primary star, and the resulting uncertainties, will be provided in another paper (Hillier et al., in preparation).

The stellar parameters and abundances model are listed in Tables 3 and 4. While the model provides a reasonable match to the optical spectrum, a comparison of the predicted UV spectrum to the observed spectrum shows a very poor match. This is primarily due to the influence of the companion star, which carves out a cavity in the wind of the primary star (Groh et al. 2012a). During most of the orbit, it is believed that we are looking at  $\eta$  Car-A through this cavity, which has an ionization structure and a density different from those of the

**Table 3**  
Star and Wind Parameters Used in Model

Parameter	Value
$L$	$4.0 \times 10^6 L_{\odot}$
$\dot{M}$	$8.0 \times 10^{-4} M_{\odot} \text{ yr}^{-1}$
$R$ ( $\tau = 10$ )	$1.28 \times 10^2 R_{\odot}$
$R$ ( $\tau = 2/3$ )	$7.42 \times 10^2 R_{\odot}$
$T_{\text{eff}}(\tau = 10)$	$2.28 \times 10^3 \text{ K}$
$T_{\text{eff}}(\tau = 2/3)$	$9.47 \times 10^2 \text{ K}$
$V$ ( $\tau = 10$ )	$5.4 \times 10^1 \text{ km s}^{-1}$
$V$ ( $\tau = 2/3$ )	$3.57 \times 10^2 \text{ km s}^{-1}$
$V_{\infty}$	$4.20 \times 10^2 \text{ km s}^{-1}$

**Table 4**  
Model Abundances

Species	Rel. Num. Fraction	Mass Fraction
H	5.0	0.547
He	1.0	0.438
C	$1.7 \times 10^{-4}$	$2.23 \times 10^{-4}$
N	$6.8 \times 10^{-3}$	$1.04 \times 10^{-2}$
O	$1.0 \times 10^{-4}$	$1.75 \times 10^{-4}$
Al	$2.2 \times 10^{-5}$	$6.36 \times 10^{-4}$
Si	$2.9 \times 10^{-4}$	$8.77 \times 10^{-4}$
Fe	$2.5 \times 10^{-4}$	$1.53 \times 10^{-3}$
Ni	$1.1 \times 10^{-5}$	$7.32 \times 10^{-5}$

primary wind. The secondary star can also modify the ionization structure of the primary wind via its UV radiation. The main consequence of the above two effects is that the absorption spectrum, in particular that due to Fe II, is much stronger in the model than in the observations. For UV data taken by HST in the late 1980s and 1990s, there was an additional effect. The coronagraph (herein referred to as the occulter) was blocking much of the stellar UV light from reaching us, and what we observed was mostly the outer halo around the binary system (Hillier et al. 2003). Fortunately, the coronagraph has much less influence today.

For this paper, we took into account the cavity carved into the wind of  $\eta$  Car-A's wind using the analytical model of Cantó et al. (1996). To compute the location of the cavity, and its shape, we assumed a mass-loss rate of  $1.0 \times 10^{-5} M_{\odot} \text{ yr}^{-1}$  and a terminal velocity of  $3000 \text{ km s}^{-1}$  for the secondary (Pittard & Corcoran 2002). In the cavity, we simply reduced the opacities and emissivities of the primary wind by a factor of 100. We made no attempt to include the secondary star and its wind, nor the bow shock.

We then took the pre-existing model and used a 2D radiation transfer code to compute the observed spectrum as a function of inclination, where (for our axisymmetric system) an inclination of zero degrees means that we are looking along the binary plane of the system with star B in the foreground. Our approach is very similar to that of Groh et al. (2012a). Crudely, the resulting spectra fall into two classes—those where we look through the cavity and those where we look only through the primary wind. It is the former that gives the best agreement with observations.

The aim of our work was not to produce a fit to the UV spectrum—rather it was designed to give a theoretical spectrum that could be used to help interpret the complex UV spectrum that we observe. Given the simplicity of the approach, and the

<sup>19</sup> An example is a foreground cloud at  $+87 \text{ km s}^{-1}$  that is seen in Si II  $\lambda 1527$  and Al II  $\lambda 1671$ .

<sup>20</sup> The C II  $\lambda 1335$  resonant line is a blend of three C II lines (Table 2):  $1334.532 \text{ \AA}$ ,  $1335.733 \text{ \AA}$ , and a much weaker line,  $1335.663 \text{ \AA}$ . The latter two components lie within  $14 \text{ km s}^{-1}$  of each other, so they are treated as a single line in the present paper.



neglect of the influence of the bow shock and the secondary UV radiation, it provides a surprisingly good match to the UV spectrum. Its main deficiencies are that it does not explain the S IV and C IV P Cygni profiles, nor absorption velocities that exceed  $\sim -500 \text{ km s}^{-1}$ .

At periastron, the secondary star moves behind the primary and does not carve a cavity in the wind of the primary. Thus, one might naively expect that the model spectrum would closely resemble that at periastron. This is true for many optical lines, but not for the UV and H $\alpha$ . The UV and H $\alpha$  formation region is large (Hillier et al. 2001, 2003) and the flow timescales need to be allowed for. For example, at  $V_\infty = 500 \text{ km s}^{-1}$ , 30 au (or  $\sim 100 R_*$ ) corresponds to a flow timescale of approximately 100 days.

#### 4.3. The Ni II $\lambda 1455$ Line

In this section, we examine changes in Ni II  $\lambda 1455$ , an example of a broad P Cygni low-ionization resonant line originating in the primary wind. We discuss higher-velocity, broad absorptions in both low- and high-ionization resonant lines that originate from the wind–wind interactions and the secondary wind at velocities of  $-600$  to  $-2600 \text{ km s}^{-1}$ . Figure 3 shows the Ni II  $\lambda 1455$  line at  $\phi = 13.194$  along with a model using CMFGEN (see Section 4.2). Although it is one of the very few relatively isolated wind lines in the FUV spectrum of  $\eta$  Car, CMFGEN modeling indicates that iron lines from the primary’s wind still influence the profile, and absorptions from intervening ejecta and interstellar gas also contribute. The red tracing in Figure 3 is the full CMFGEN spectrum, and the blue tracing isolates the iron contributions that dominate the UV spectral region.

From Table 2, the first and second ionization energies of nickel are 7.64 eV and 18.17 eV, below and above the ionization potential of hydrogen (13.6 eV). This resonant line provides a means of tracking the lower ionization boundary of the primary wind and the ionized ejecta within the Homunculus and Little Homunculus. The line shows broad, unsaturated absorptions extending from 0 to  $-600 \text{ km s}^{-1}$  with a broad emission component that peaks around  $+200 \text{ km s}^{-1}$ , extending redward to  $+500 \text{ km s}^{-1}$ . The large offset of the emission peak velocity is most likely due to blending with low-velocity absorption.

Figure 4 compares two profiles of Ni II  $\lambda 1455$ . Narrow absorptions are seen at  $-513 \text{ km s}^{-1}$  (arising in the expanding Homunculus) and at  $-146 \text{ km s}^{-1}$  (arising from the Little Homunculus, Gull et al. 2005). The P Cygni profile peaks at  $+200 \text{ km s}^{-1}$  with an unsaturated absorption reaching minimum near  $-300 \text{ km s}^{-1}$  in spectra at phases  $\phi = 10.818$  and 13.886 (i.e., at nearly the same orbital phase 16.6 years apart). Four narrow Ni II  $\lambda 1455$  absorption systems are in our LOS: one interstellar,  $+4 \text{ km s}^{-1}$  and three absorptions from ejecta shells arising from the Little Homunculus (at  $-146 \text{ km s}^{-1}$ ), the Homunculus (at  $-513 \text{ km s}^{-1}$ ), and near the Homunculus,  $-489 \text{ km s}^{-1}$  (Nielsen et al. 2005).

While the  $-146 \text{ km s}^{-1}$  component disappeared by  $\phi = 13.886$ , some weaker, singly ionized metal lines briefly returned during periastron passage 14. The optical resonance line, Na D, is discussed by Pickett et al. (in prep), who found that the  $-146 \text{ km s}^{-1}$  component weakened after 2009 (periastron passage 11) and disappeared in 2015 and 2016 (following periastron passage 12), while a  $-168 \text{ km s}^{-1}$

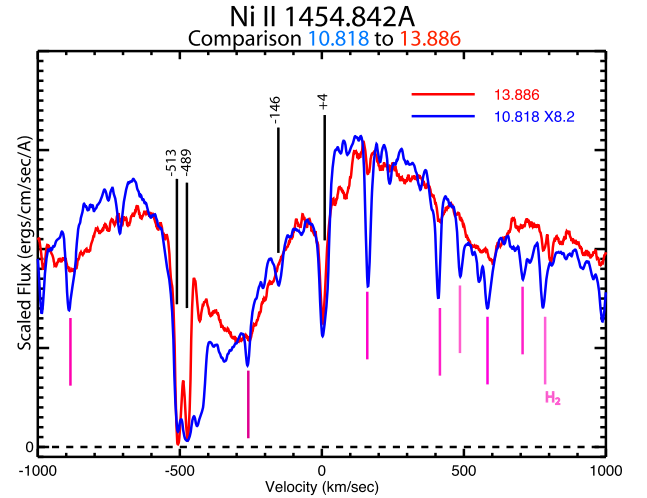


**Figure 4.** Ni II  $\lambda 1455$  velocity plots at similar binary phases of  $\phi = 10.818$  and  $\phi = 13.886$ . The flux of the  $\phi = 10.818$  spectrum has been scaled to the flux at  $\phi = 13.886$  at  $\lambda = 1483 \text{ Å}$ , a relatively line-free portion of the spectrum. Between the two observations, 16.5 years apart, the apparent flux has increased by a factor of 8.2. The increase in FUV flux led to the disappearance of (1) H $_2$  absorptions at  $-512 \text{ km s}^{-1}$  (Homunculus) and (2) Ni II  $\lambda 1455$  absorptions at  $-146 \text{ km s}^{-1}$  (Little Homunculus) and from  $-250$  to  $-475 \text{ km s}^{-1}$  from the multiple shells within the Homunculus and Little Homunculus. Strong absorption remained at  $-486$  and  $-513 \text{ km s}^{-1}$ , the stronger shells at the boundary of the Homunculus. The shape of the P Cygni wind profile has not changed significantly.

component appeared briefly during the 2020 periastron passage.

Eight narrow lines of H $_2$  at  $-513 \text{ km s}^{-1}$  are present in the  $\phi = 10.818$  velocity plot but are not seen at  $\phi = 13.886$ . These absorptions are members of the ultraviolet Lyman bands. Ten percent of the band transitions lead to molecular dissociation (Dalgarno & Stephens 1970; Jura 1974). Model calculations by Werner (1969), scaled to the changing radiation field within the Homunculus, suggest that the dissociation lifetime of  $N_{H_2}$  dropped from a century to a decade between 2002 and 2019, likely the direct result of the tenfold increase in FUV radiation. Across periastron passage 11, the H $_2$  absorptions briefly disappeared, but returned by phase 11.119 (Nielsen et al. 2005). The transient disappearance of H $_2$  absorptions is due to absorption of the FUV flux (necessary to populate upper H $_2$  levels) by the intervening primary wind across the periastron passage.

The disappearance of lines of singly ionized elements across the high-ionization state occurred because of the increase in ionization (e.g., Ni $^+$  to Ni $^{++}$ , Ti $^+$  to Ti $^{++}$ , etc.) due to the increased photoionizing radiation in our LOS. The increase in photoionizing radiation field has produced many changes in the narrow-line absorption spectra since periastron 11 in 2003.5. Details of the changes in the multiple shells are a topic for another paper (Nielsen et al., in prep). Despite the dramatic increase in the overall UV flux level, the P Cygni profiles have not substantially changed (after allowing for the high-velocity components from the several shells within the Homunculus along the LOS).

#### 4.4. Comparison of Ni II $\lambda 1455$ Changes between Periastron Passages 11 and 14

In this section, we study the behavior of Ni II  $\lambda 1455$  across periastron passages 11 and 14. Due to variations in continuum



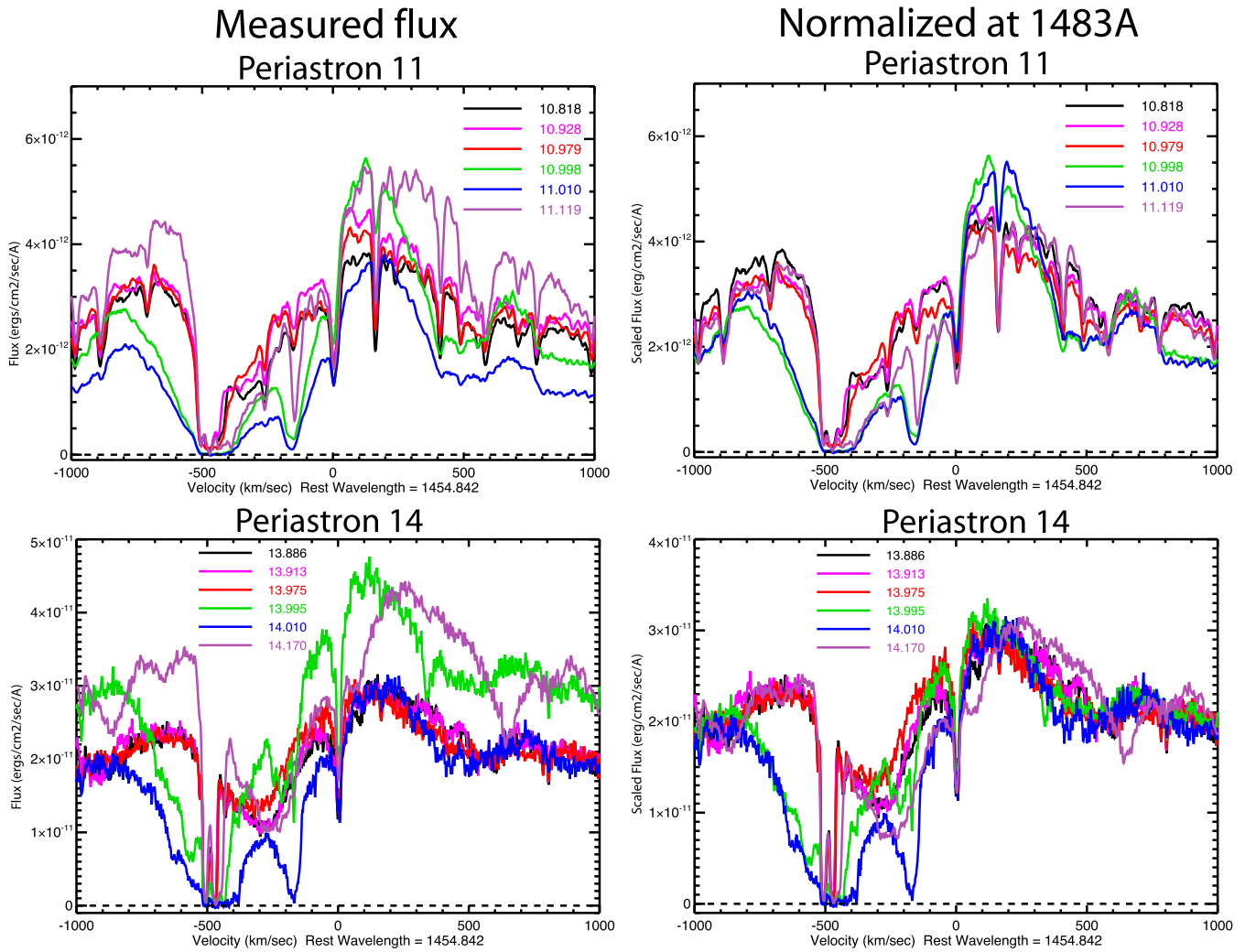


**Figure 5.** Velocity profiles of Ni II  $\lambda 1455$  changing across periastron passages 11 (top row) and 14 (bottom row). Profiles plotted in the left column change in amplitude due to the changing continuum levels. Profiles in the right column have been normalized to the continuum level near 1483Å (1475 to 1490 Å). The normalized profiles (right column) show very little change leading up to periastron (10.818, 10.928, 10.979; 13.886, 13.913, 13.975) but change dramatically across periastron passage (10.998, 11.010; 13.995, 14.010) where there is a general enhancement in absorption, with extended absorption from  $-500$  to  $-800$  km s $^{-1}$  now present. Profiles are returning to the pre-periastron values by phases 11.119 and 14.170.

flux both within an orbital cycle and over longer timescales, Figure 5 shows the Ni II  $\lambda 1455$  profiles in two ways: In the left column, the profiles are displayed in absolute flux, while in the right column, the spectra are scaled by the measured continuum from 1475 to 1490 Å, which shows minimal spectral changes over an orbital period (Groh et al. 2010).

Direct comparison of the profiles at each phase is complicated by the changes in flux between cycles 10 and 13 and the changes in the strength of the absorptions arising in the Homunculus and Little Homunculus. However, a comparison of flux-scaled profiles (Figure 5, right column) reveals that, despite the nearly tenfold change in flux, the overall shapes of the profiles near the high-ionization state are similar, as are profiles in the low-ionization state (near  $\phi = 11.01$  and  $\phi = 14.01$ ).

The scaled spectra provide much clearer views of the changes in the resonant line profile across periastron passages 11 and 14. By  $\phi = 10.998$  (13.995), strong, broad absorption developed blueshifted beyond  $-600$  km s $^{-1}$ , extending to  $-800$  km s $^{-1}$ . This broad absorption disappeared in the recovery stages in both cycles ( $\phi = 11.119$  & 14.022). The

continuum-normalized profiles are sensitive to changes in ionization of the colliding wind bow shock, so the similarity in profile shape between cycle 11 and cycle 14 suggests little change in ionization state of the wind–wind collision.

Across periastron 11 (Figure 5, top left), the continuum UV flux declined by  $\phi = 11.010$  but brightened by  $\phi = 11.119$ , to higher levels than those measured at  $\phi = 10.979$  (Gull et al. 2021). In contrast, across periastron 14 (Figure 5, bottom left), the continuum increased by  $\phi = 13.995$ , faded somewhat by  $\phi = 14.010$ , and recovered to pre-periastron flux level by  $\phi = 14.022$ .

Some orbit-related changes in the UV in each cycle are linked to the “borehole” effect (Madura & Groh 2012; Gull et al. 2021), a cavity deep in the inner wind of  $\eta$  Car-A near periastron passage, produced when  $\eta$  Car-B enters the inner wind of  $\eta$  Car-A, which exposes deeper, hotter layers of  $\eta$  Car-A and thus leads to an increase in ionizing continuum for a brief interval. The borehole produces a strengthening of the redshifted broad emission across both periastron passages in the velocity range from  $+50$  to  $+300$  km s $^{-1}$  when the extended wind moves into the borehole cavity. Eventually,

the primary wind then fills in the borehole and the redshifted emission drops toward equilibrium. The similarity of the borehole effect in the two cycles suggests that the intrinsic flux from the inner regions of  $\eta$  Car-A has not changed appreciably in the 16 years separating the two orbital cycles.

Ionization of Ni to  $\text{Ni}^+$  (IP = 7.6 eV) is easily provided by UV radiation from  $\eta$  Car-A. However, ionization of  $\text{Ni}^+$  to  $\text{Ni}^{+2}$  (IP = 18.2 eV) requires photons below the Lyman limit. CMFGEN models suggest that  $\text{Ni}^{+2}$  predominates within the inner wind of  $\eta$  Car-A ( $r < 15$  au), but  $\text{Ni}^{+2}$  absorption is not easily seen against the continuum of  $\eta$  Car-A. Due to the atomic structure of Ni III, no strong resonant lines are found above 910 Å.

As the EUV from  $\eta$  Car-B drops near periastron passage,  $\text{Ni}^{+2}$  in the Little Homunculus and Homunculus recombines, leading to nearly saturated  $\text{Ni}^{+1}$  absorption from  $-140$  to  $-500 \text{ km s}^{-1}$ . Near  $\phi = 11.01$  and  $\phi = 14.01$ , the absorption profile is saturated between  $-400$  and  $-500 \text{ km s}^{-1}$ , with a high-velocity blue wing extending to  $-900 \text{ km s}^{-1}$  (Figure 5). This high-velocity absorption wing occurs when the accelerated wind of the primary crosses our LOS as  $\eta$  Car-B moves around  $\eta$  Car-A (Figure 1-C). By  $\phi = 11.119$  and  $\phi = 14.170$ , the transient absorptions disappear once the EUV radiation reionizes the foreground shells and the previously formed cavity. The newly formed cavity is bounded by a new downstream bow shock composed of accelerated primary wind that flowed across periastron passage.

## 5. Epoch-dependent Variations in Profiles at Similar Phase

Line profiles near the same phase in different orbital cycles provide key diagnostics that aid in understanding the long-term changes in the foreground structures and constraining intrinsic changes to the stars themselves. In this section, we constrain non-orbit-related changes in the line profiles by comparing line profiles at similar orbital phases in different orbital cycles. Because of the complex absorption spectrum arising from intrinsic wind and foreground structures, we can examine the behavior of doublet lines to constrain effects of blending that can affect the shapes of the absorption lines. We also compare the observed spectra to model spectra, to further disentangle the observed profiles.

### 5.1. A Comparison of Three Epochs in the Early High-ionization State

A fundamental question is whether the binary winds have changed substantially across the interval sampled by HST/STIS observations. Any such changes would indicate intrinsic variations in  $\eta$  Car-A and/or  $\eta$  Car-B. To address this question, we compare wind profiles at three similar orbital phases in three different orbital cycles:  $\phi = 11.119$ ,  $13.194$  and  $14.170$ . At these phases, the ionization of the wind structures has almost fully recovered to the high-ionization state near apastron, and the influence of  $\eta$  Car-B on the inner primary wind is minimal (Hillier et al. 2001, 2006). Figure 6 compares the profiles of six resonance lines that have been normalized relative to the “continuum” at  $\phi = 14.170$  in the 1475 to 1490 Å region, a wavelength region that has few absorption features. These normalized profiles are astonishingly similar, despite the very different flux scaling factors:  $8.25 \times (\phi = 11.119)$ ,  $1.54 \times (\phi = 13.194)$  and  $1.00 \times (\phi = 14.170)$ . Closer examination of the FUV spectra shows that the narrow line absorptions of  $\text{H}_2$  ( $-513 \text{ km s}^{-1}$ ) greatly weakened between 11.119 and

13.194, and are nearly absent by 14.170 (Section 4.1). Most narrow, low-ionization absorption lines over the velocity interval from  $-120$  to  $-180 \text{ km s}^{-1}$  have also weakened or disappeared. These changes were caused by the nearly tenfold increase in FUV flux on the foreground absorbers. Fewer changes in the singly ionized metal absorptions occurred blueward of  $-400 \text{ km s}^{-1}$ , but  $\text{H}_2$  at  $-513 \text{ km s}^{-1}$  was destroyed. By  $\phi = 14.170$ , EUV radiation further ionized the Little Homunculus ( $-146 \text{ km s}^{-1}$ ), but had not yet strongly affected the Homunculus shell ( $-513 \text{ km s}^{-1}$ ), and the increase in radiation longward of 912 Å caused the photodestruction of  $\text{H}_2$  in our LOS in the most recent spectra.

The bulk of changes in broad absorption occurred in the  $-120$  to  $-400 \text{ km s}^{-1}$  velocity range. Absorption in Al II, Al III, and Si II decreased with time most strongly between  $\phi = 11.119$  and  $13.194$  across that velocity interval. These changes are due to enhanced ionizing flux, which indicates that the affected structures reside within or beyond the occulter relative to the position of  $\eta$  Car in our LOS. Some decrease in absorption is present in the C II profile. However, the C II doublet overlaps by  $1.17 \text{ Å}$  ( $V = 284 \text{ km s}^{-1}$ ), which complicates the tracking of detailed changes in absorption by the individual C II lines. The blue component of the Si IV doublet ( $\lambda 1394$ ) shows a P Cygni profile that is similar at all three phases. However, at  $\phi = 11.119$ , the strong absorption in the  $-120 < V < 600 \text{ km s}^{-1}$  range is not saturated, but it is saturated at the two following phases.

The overlap of the C IV doublet ( $1.59 \text{ Å}$  or  $498 \text{ km s}^{-1}$ ) is comparable to the velocity range of interest and possibly contaminated by other species (see Section 5.3), so the profile is challenging to interpret. At phase 11.119, for example, the blue component is unsaturated while the red component, which has the lower  $gf$  value, appears to be saturated. However, with knowledge of the intervening absorbing structures, contributions can be parsed out of these overlapping velocity intervals. At  $\phi = 11.119$ , the absorptions of  $\lambda\lambda 1548, 1550$  at  $-500 \text{ km s}^{-1}$  are strong and moderately wide, but not saturated. At  $\phi = 13.194$ , the  $\lambda 1548$  absorption broadened relative to the  $\lambda 1550$  absorption and relative to the  $\lambda 1548$  absorption at  $\phi = 11.119$ . By  $\phi = 14.170$ , both  $\lambda\lambda 1548, 1550$  profiles again narrowed and had similar red shoulders.

### 5.2. Comparing Doublet Profiles

By comparing doublet line-profiles, we can disentangle absorption contributions from other lines to obtain information about absorption optical depths and covering factors. In the optically thin case, the absorption depths of the doublet members scale as the  $gf$  value (Table 2), but at large optical depths, both lines become saturated. If two lines with different  $gf$  values show identical nonzero absorption profiles, the covering factor is likely less than unity (assuming a negligible line source function).

Figure 7 displays profiles of six strong doublets for the same three spectra recorded in early recovery to the high-ionization state discussed in Section 5.1. As noted by Hillier et al. (2001, 2006), the influence of  $\eta$  Car-B on the atmosphere and inner wind of  $\eta$  Car-A is minimal (from our perspective) in the early recovery phase. In the three orbital phases shown in Figure 7, the doublet profiles from  $0$  to  $-600 \text{ km s}^{-1}$  are nearly identical for Si II and Al III. However, there are important differences for the two species. The Al III profiles show an absorption reversal near  $-500 \text{ km s}^{-1}$  at  $\phi = 13.194$ , and especially at  $\phi = 14.170$ . This reversal is larger for the red component, and is consistent with the

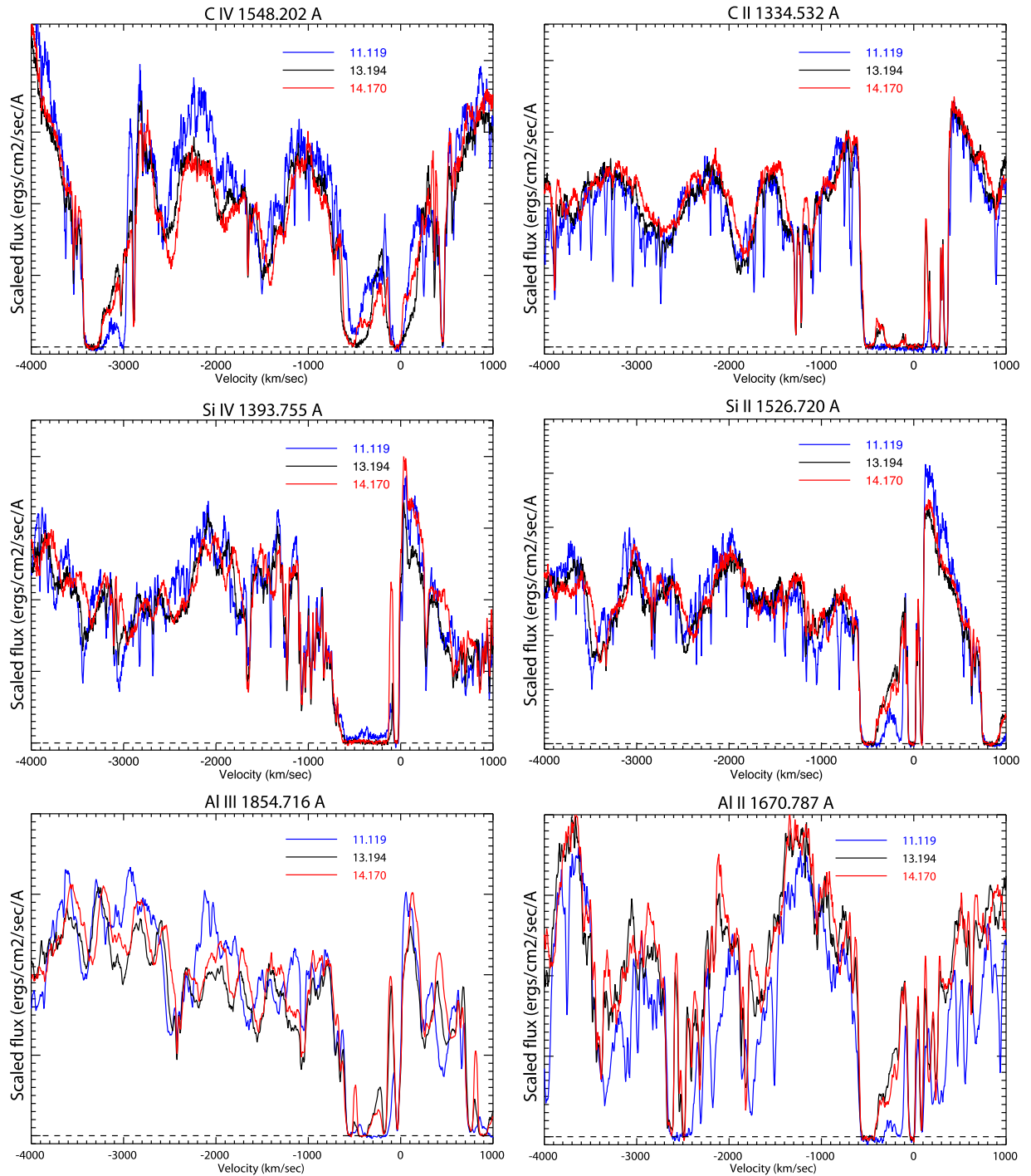


**Figure 6.** Normalized velocity plots of six strong resonant lines recorded at similar orbital phases in the early recovery to the high-ionization state. The C IV and C II doublets are separated by only 498 and 284  $\text{km s}^{-1}$ , resp., in velocity space, which leads to significant overlap in the 0 to  $-500 \text{ km s}^{-1}$  velocity range of interest. C II, Si II, and Al II reveal decreased absorption after periastron 13, due to the increased FUV radiation leading to multiply ionized shells within the Homunculus and the Little Homunculus. Lesser changes in absorption are apparent in Al III, but a long-term drop in absorption appears to occur at about  $-500 \text{ km s}^{-1}$ . The C IV  $\lambda\lambda$  1548,1551 absorptions appear to broaden by  $\phi = 13.194$  then narrow at  $\phi = 14.170$ , centered on  $-500 \text{ km s}^{-1}$ . This suggests that the colliding wind structure in the LOS changes with time in an unpredictable manner. The spectra were normalized in flux relative to the continuum in the 1475 to 1490  $\text{\AA}$  spectral interval, where relatively few absorption features are apparent. Normalization factors were  $8.25 \times (\phi = 11.119, 1.54 \times (\phi = 13.194 \text{ and } 1.00 \times (\phi = 14.170)$ .

red component having the smaller  $gf$  value. Since a “normal” wind would give rise to a continuous P Cygni absorption profile, the higher-velocity Al III does not originate in the unperturbed wind of  $\eta\text{Car-A}$ . A separate absorber gives rise to the Al III centered at  $-550 \text{ km s}^{-1}$ . By contrast, the Si II profiles are nearly black from  $-400$  to  $-600 \text{ km/s}$ , especially at the two later orbits. The profile from  $-400 < V < -100 \text{ km s}^{-1}$  is similar in the

two profiles, and is broadly consistent with that expected for resonance scattering in a stellar wind plus shell absorptions at  $\approx -150 \text{ km s}^{-1}$  (analogous to the Ni II  $\lambda 1455$  velocity profile seen in Figure 4). By contrast, the profiles of the C II doublet are very different between  $-100$  and  $-400 \text{ km s}^{-1}$ . The (red)  $\lambda 1336$  absorption is noticeably weaker than the (blue)  $\lambda 1335$  absorption, again consistent with the  $gf$  values.

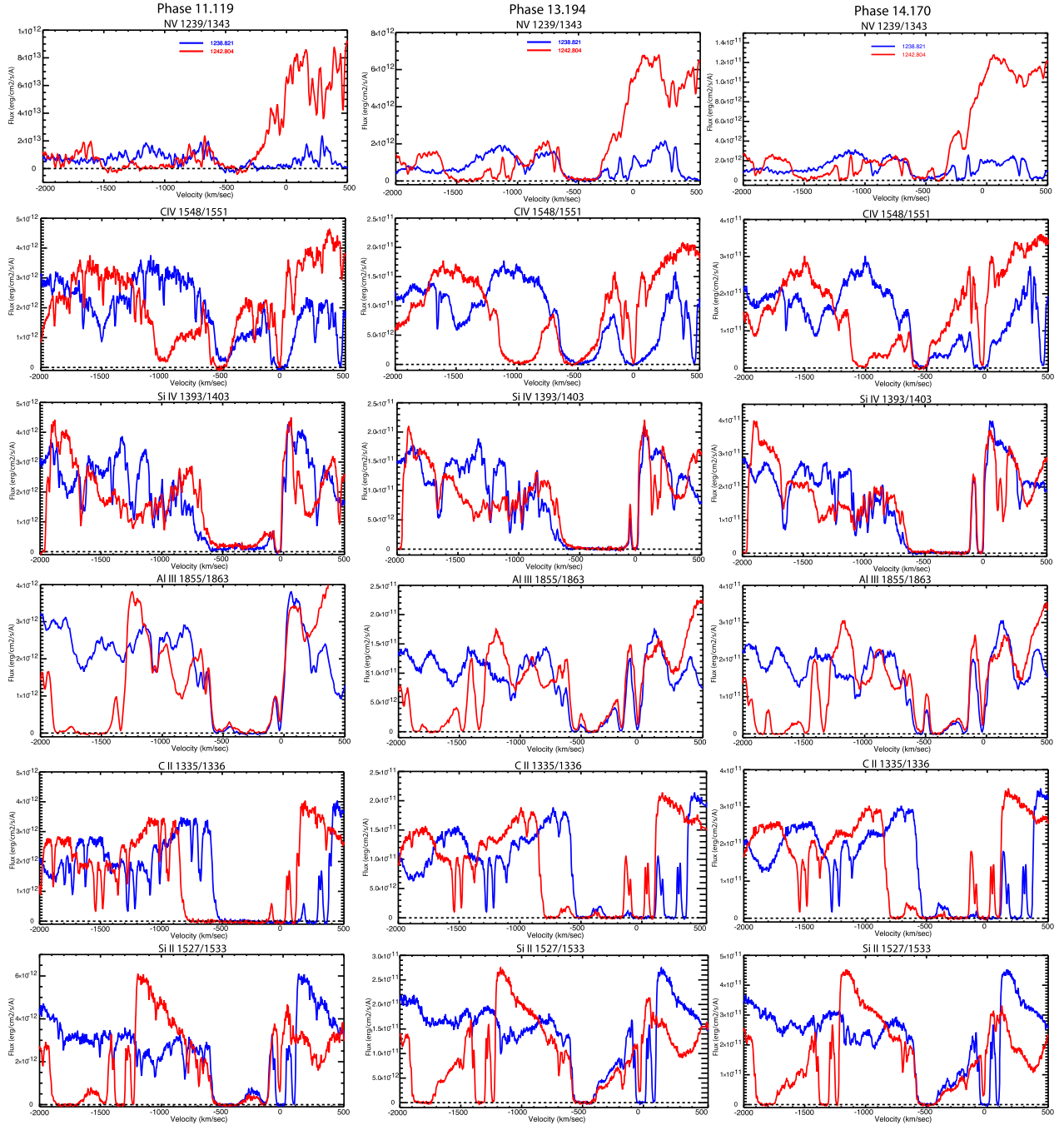


**Figure 7.** Plots of six doublet profiles recorded in three separate cycles near  $\phi = 0.15$  when the winds and multiple Homunculus/Little Homunculus shells are in early recovery to the high-ionization state. The blue member of the doublet is shown in blue and the longer-wavelength member is shown in red. For Si II and Al III, the absorption between  $-100$  and  $-600$  km s $^{-1}$  is very similar in both members of the doublet, and indicates identical maximum absorption velocities of  $\sim 600$  km s $^{-1}$ . The Si IV profiles, while similar, indicate somewhat higher velocities. A peculiar notch at  $\sim -700$  km s $^{-1}$  is present in the Si IV profiles at all three phases in both doublet members, so they must be real. As the longer doublet member absorption (red) is consistently weaker than the shorter doublet member (blue), the gas causing this absorption is not optically thick. The C IV and N V differ from their low-ionization counterparts, but the doublet components show similar (although not identical) absorption structure. A simple comparison of the C II profiles cannot be made, because of the small separation ( $\sim 280$  km s $^{-1}$ ) between the two strongest members. The  $+87$  km s $^{-1}$  absorption as seen in the shorter-wavelength line for Si II and C II is from an extensive IS cloud well in front of  $\eta$  Car, and as documented by Walborn et al. (2002), found to be present in the spectra of multiple stars within the Carina region.

The Si IV doublet absorption profile at  $\phi = 11.119$  is nearly saturated, and the red component of the doublet shows a larger residual flux from  $-100 < V < -600$  km s $^{-1}$ . This is probably due to the extended wind of  $\eta$  Car-A, which dominates the total flux at  $\phi = 11.119$ , compared to later times when the occulter dissipated and continuum from the core of  $\eta$  Car-A dominates. At  $\phi = 13.194$  and  $14.170$ , both profiles are saturated. This saturation is especially remarkable because it

means that there is highly ionized gas that covers a broad velocity range along our line of sight and that covers the entire continuum-emitting region of the binary system. The distribution of gas that produces the broad Si IV P-Cygni absorption must be asymmetric, since if it were symmetric, absorption from a normal, unperturbed stellar wind, the P-Cygni profile would more closely resemble the CMFGEN model profile of Si II  $\lambda 1533$  (Figure 8).



## Comparison of line profiles from 13.194 to CMFGEN and Fe profiles

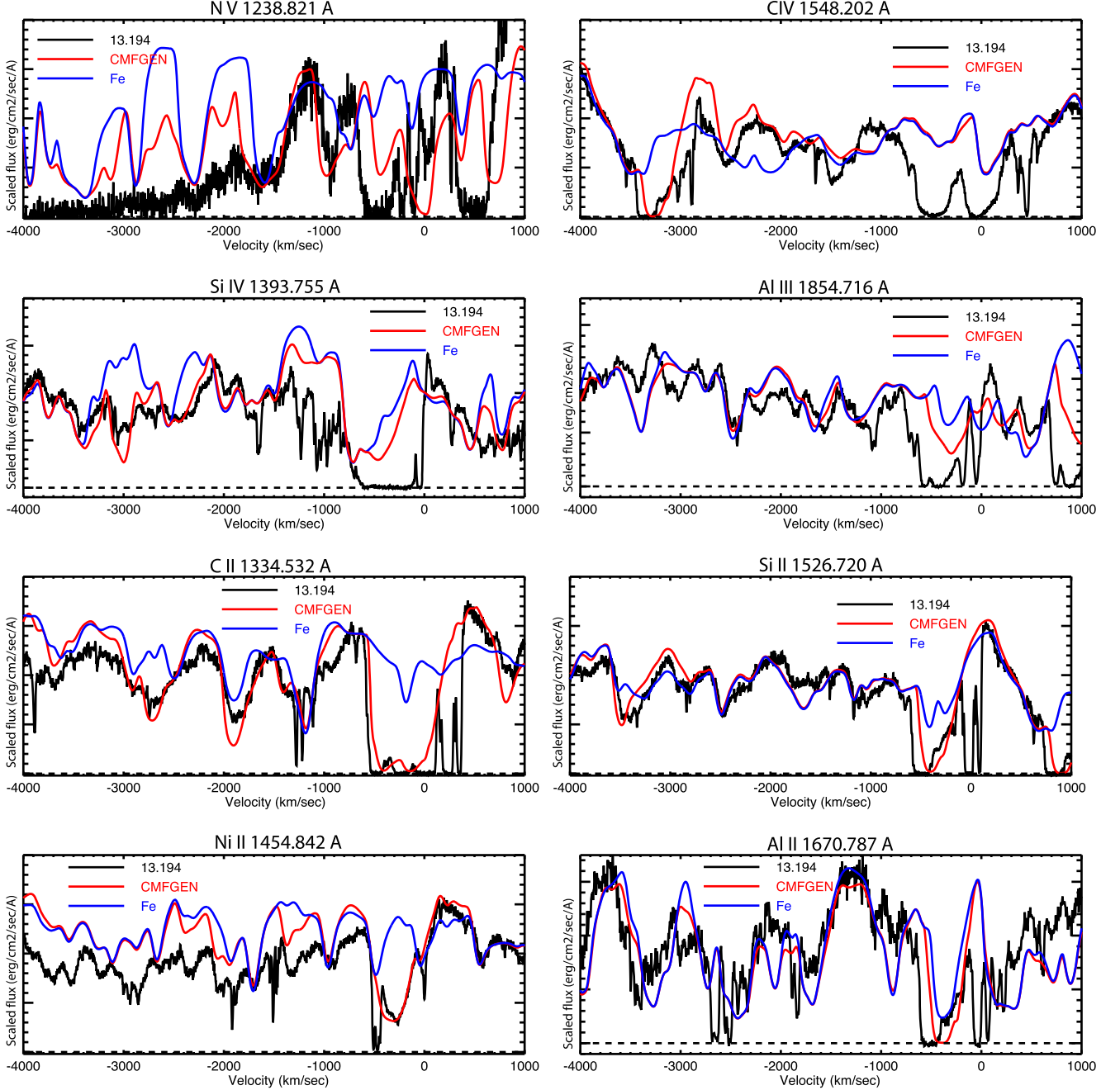


**Figure 8.** Comparison of CMFGEN model profiles with observed profiles recorded at  $\phi = 13.194$ . The CMFGEN model of  $\eta$  Car-A, which used  $V_{\infty,A} = 420 \text{ km s}^{-1}$ , accounts for the bulk of the 0 to  $-500 \text{ km s}^{-1}$  absorption for the low-ionization species up to C II, less so for Al III and Si IV, and little or no absorption by C IV and N V.

The blue-edge velocities indicate the maximum speed of the gas along our line of sight. The blue-edge profiles of Si II and for Al III are very similar, and are saturated to  $V \approx -550 \text{ km s}^{-1}$ . The profile is black only to a velocity of  $-520 \text{ km s}^{-1}$ , but the C II profile is complicated by the extreme velocity overlap of the doublet. The Si IV blue edge on the blue component of the doublet has a steeper slope than the red component, and might be attributable to optical depth effects (the blue component has a  $gf$  value that is a factor of two larger) plus incomplete coverage of the source.

The CIV doublet velocity profiles show considerable differences in the three observations. At  $\phi = 11.119$ , both lines

show deep absorption extending from about  $-500$  to  $-600 \text{ km s}^{-1}$ . However, the redder component of the doublet shows evidence for extra absorption by another species, since it is deeper, and extends to slightly higher velocities than the 1548 component, despite its  $gf$  value being a factor of two lower than the blue component. Comparisons with the CMFGEN model in Section 4.2 show that iron absorption in the spectrum of  $\eta$  Car-A contaminates the red doublet component. At  $\phi = 13.194$ , both CIV lines show strong, broadened absorption extending from  $-300$  to  $-650 \text{ km s}^{-1}$ , much broader than that seen at phases 11.119 and 14.170. At  $\phi = 14.170$ , the lines again show deep absorption extending

from about  $-500$  to  $-600$   $\text{km s}^{-1}$ , but the edge velocities are identical. Both components show absorption between  $-100$  and  $-500$   $\text{km s}^{-1}$  that is broadly consistent with the  $gf$  values, although confusion caused by line overlap could play a role. The broad component of  $\lambda 1550$  obscures the  $-40$   $\text{km s}^{-1}$  component of  $\lambda 1548$ . But the  $\lambda 1550$   $-40$   $\text{km s}^{-1}$  narrow component is present, confirming strong, well-defined absorption at that velocity, which is characteristic of Weigelt clumps B, C, and D (Gull et al. 2016).

We confirm the presence of the NV doublet from the broad, nearly saturated absorption extending from  $-300$  to  $-600$   $\text{km s}^{-1}$  in both doublet components (velocity separation of  $915$   $\text{km s}^{-1}$ ) in all three observations. However, the profile is noticeably broader at  $\phi = 11.119$  than at  $13.194$  and  $14.170$ . As noted by Gull et al. (2021), the wavelength-dependent absorption steepens below  $1300$  Å, so the NV profiles were normalized at  $1250$  Å for comparison.

### 5.3. Comparing Observed and Model Profiles

We now compare early recovery profiles just after periastron passage to model profiles of  $\eta$  Car-A from CMFGEN (Section 4.2) to estimate the contribution of the primary wind to the observed profiles, and to identify possible contributions from  $\eta$  Car-B, the colliding winds, and the discrete foreground shells within the Homunculus.

Figure 8 compares profiles at  $\phi = 13.194$  with CMFGEN model profiles (shown in red), along with the expected contribution of iron to the spectrum (in blue). Isolating the iron spectrum helps identify most of the contaminating primary wind absorptions near the resonant lines of interest. As shown in Section 4.3, the CMFGEN model spectrum produces a velocity profile for Ni II that is very similar to the observed velocity profile (Figure 8, lower left), and helps identify the  $+4$  and  $-500$   $\text{km s}^{-1}$  absorptions as arising from an interstellar cloud and the Homunculus, respectively (see Figure 4). In general, the models show a significant primary wind contribution to low-ionization lines (C II, Al II, and Si II), but little or no contribution to the high-ionization lines (Si IV, C IV, and N V). For the low-ionization species, the CMFGEN profiles extend to about  $\sim -420$   $\text{km s}^{-1}$  as expected for the primary wind; however, the observed profiles are saturated out to  $V \sim -550$   $\text{km s}^{-1}$ .

Figure 9 compares the doublet profiles from the CMFGEN model with the observed profiles. The observed doublet profiles are quite similar from NV (IP =  $77.47$  eV) through Si II (IP =  $8.15$  eV), which reinforces the idea that the absorptions originate from the specific resonant lines. However, the doublet profiles from the CMFGEN model are similar only for the low-ionization lines (Si II and C II). The CMFGEN model also shows weak Al III P Cygni absorption. The CMFGEN profile of the Al III doublet may be contaminated by iron absorption, which could be due to the influence of  $\eta$  Car-B on the outer wind of the  $\eta$  Car-A.

### 5.4. Long-term Changes

To constrain long-term (non-orbit-related) changes in the system, we compare spectra at nearly the same phase in the velocity range of  $-4000$  to  $+1000$   $\text{km s}^{-1}$  for select lines (Figures 10 through 13). Following Groh et al. (2010), for our comparison, we normalized the spectra to the continuum near  $1487$  Å ( $\lambda\lambda 1475$  to  $1490$ ). However, we used the continuum near

$1800$  Å ( $\lambda\lambda 1775$  to  $1805$ ) when scaling the aluminum doublet, as the observations were done with the E230M echelle.

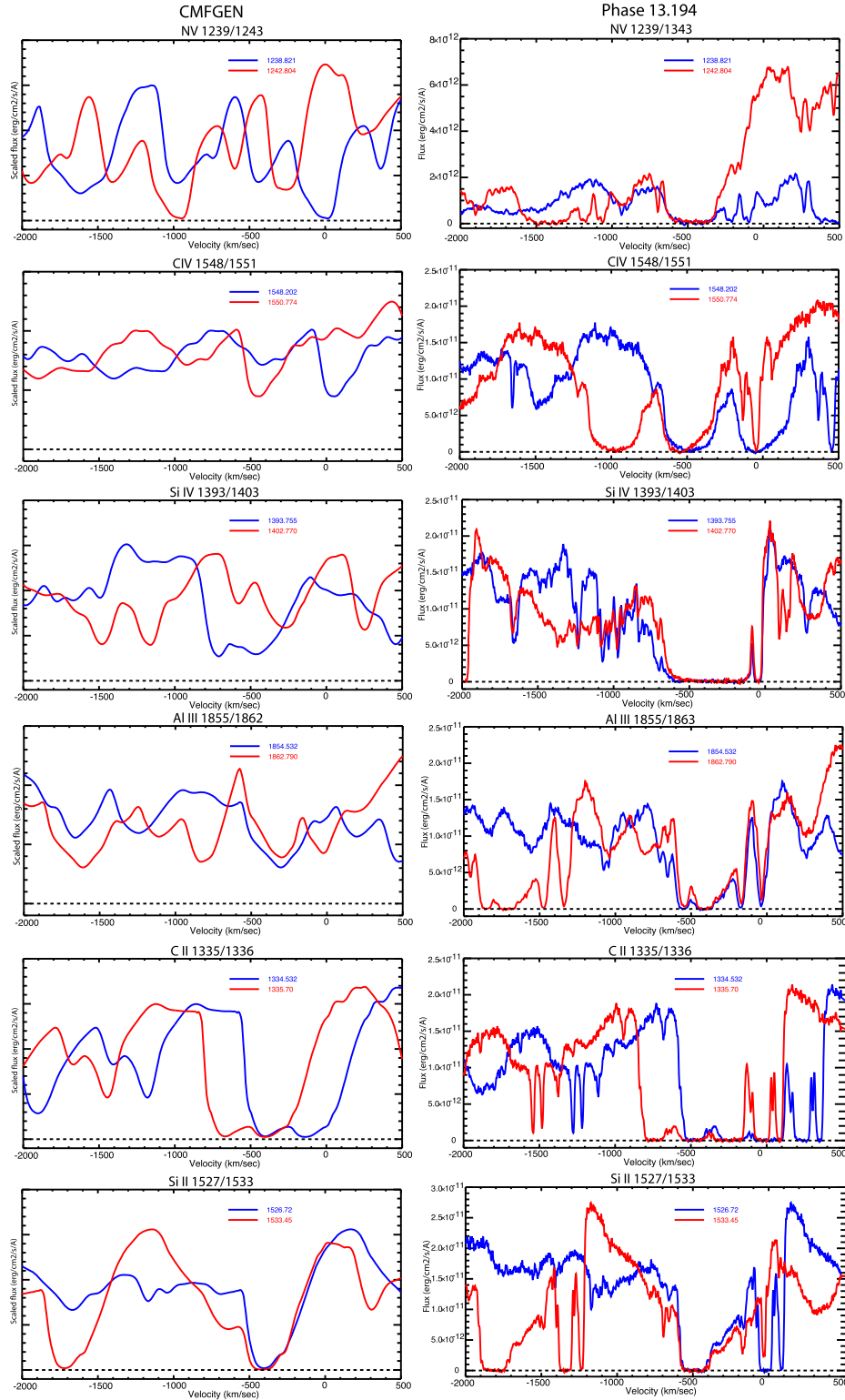
#### 5.4.1. Comparison of C IV and C II Resonant Line Profiles

Figure 10 compares C IV  $\lambda 1548$  (IP =  $64.5/392$  eV) and C II  $\lambda 1335$  (IP =  $11.3/24.4$  eV) at nearly the same orbital phases from cycles 10/11 and 13/14. The normalized C II profiles leading up to periastron passages 11 and 14 ( $\phi = .703$  to  $.977$ ) are surprisingly similar throughout the entire velocity range  $-600 < V < -4000$   $\text{km s}^{-1}$ , as well as in the early recovery to high-ionization state after periastron passages ( $\phi = 1.145$ ). Near the periastron passage in orbital cycle 14 ( $\phi = 13.995$  &  $14.010$ ), the C II profile shows a blue absorption wing extending from  $-1000 < V < -600$   $\text{km s}^{-1}$  that was not present during periastron passage 11. This wing largely disappeared by  $\phi = 14.022$  and fully disappeared by  $\phi = 14.170$ , when there once again was good agreement between the normalized line profiles from cycle 14 and cycle 11.

Because the velocity spacing between C II  $\lambda 1335$  and  $\lambda 1336$  is only  $284$   $\text{km s}^{-1}$ , the spectral component are blended, which complicates the comparison of C II with C IV  $\lambda\lambda 1548, 1555$ . Small “continuum” bumps visible between  $0$  and  $-600$   $\text{km s}^{-1}$  during the high-ionization state disappear near periastron passages in both cycles. This change is likely due to a change in ionization—the carbon in some shells is multiply ionized during the high-ionization state but returns to a less-ionized state near periastron passage.

The blue absorption wing that appeared in C II near periastron passage 14 is very similar to the wing seen in three Si II doublet profiles shown in Gull et al. (2021). They suggested that the repetition of this blue absorption wing in Si II is likely caused by dense clumps of material in the trailing arm of the bow shock that move into our LOS during periastron passage. Pittard (2007) modeled interactions of clumps with wind–wind shocks and determined that the clumps are rapidly destroyed. The transient blue-absorption wing we see for about 70 days around periastron passage may be an example of clump destruction in the bow shock on this timescale.

The changes seen in the C IV profile are similar to those seen in the C II line. The C IV line also shows a blue absorption wing near periastron in cycle 14 at the same phases where the blue wing is seen in the C II line. The C IV blue wing in cycle 14 extends from velocities between  $-100 < V < -1400$   $\text{km s}^{-1}$ , and probably to  $-2600$   $\text{km s}^{-1}$  (which is near the expected terminal velocity of the wind of  $\eta$  Car-B). Groh et al. (2010), using the same HST/STIS spectra recorded before periastron passage 11, identified a transient absorption extending to  $-1200$   $\text{km s}^{-1}$ , and also showed transient high-velocity absorption in He I  $\lambda 10830$  extending to  $-1900$   $\text{km s}^{-1}$ . The C IV absorption extending to  $-2600$   $\text{km s}^{-1}$  suggests that our LOS extends deeper into the wind–wind structure, due to the disappearing occulter. This is in line with the greatly increased FUV flux and the apparent decrease of the H $\alpha$  equivalent width over the past few decades (Mehner et al. 2012, 2015; Damineli et al. 2021). However, the extended blue absorption wing seen in C IV may be blended with other variable absorptions near periastron passage, especially at the most blueward velocities. In contrast to C II, high-velocity absorption is also present in C IV from  $-100$  to  $-2600$   $\text{km s}^{-1}$  at  $\phi = 0.703$  in cycle 14. The absorption appears to be in two velocity intervals, from  $-100$  to  $-1500$   $\text{km s}^{-1}$  and then between  $-2000$  to  $-2600$   $\text{km s}^{-1}$ . This suggests that both the C IV  $\lambda 1548$  and  $\lambda 1551$  lines are absorbing in the  $-2000$  to  $-2600$   $\text{km s}^{-1}$  velocity range in addition to the  $-500$  to  $-600$   $\text{km s}^{-1}$  interval.



**Figure 9.** Comparison in velocity space of six doublet pairs from the CMFGEN mode (with  $V_{\infty A} = 420 \text{ km s}^{-1}$ , left column) and observed doublet pairs from the  $\phi = 13.194$  spectrum (right column). In the model,  $\eta$  Car-A contributes a significant wind absorption between 0 to  $-500 \text{ km s}^{-1}$  for low-ionization lines from Si IV and negligible absorption for C IV or N V. The shorter-wavelength line of the doublet is plotted in blue, and the longer-wavelength line is plotted in red.

#### 5.4.2. Comparison of Si IV and Si II Doublet Absorptions

The normalized Si IV (IP = 33.5/45.1 eV) and Si II (IP = 8.2/16.4 eV) profiles are displayed in two separate figures, as the doublet lines are separated sufficiently to allow independent

comparisons of the lower velocity range (Figures 11 and 12). Indeed, the shorter-wavelength members of the two doublets have no competing strong absorptions up to  $-4000 \text{ km s}^{-1}$ , well beyond the expected terminal velocity of  $\eta$  Car-B (Pittard & Corcoran 2002).

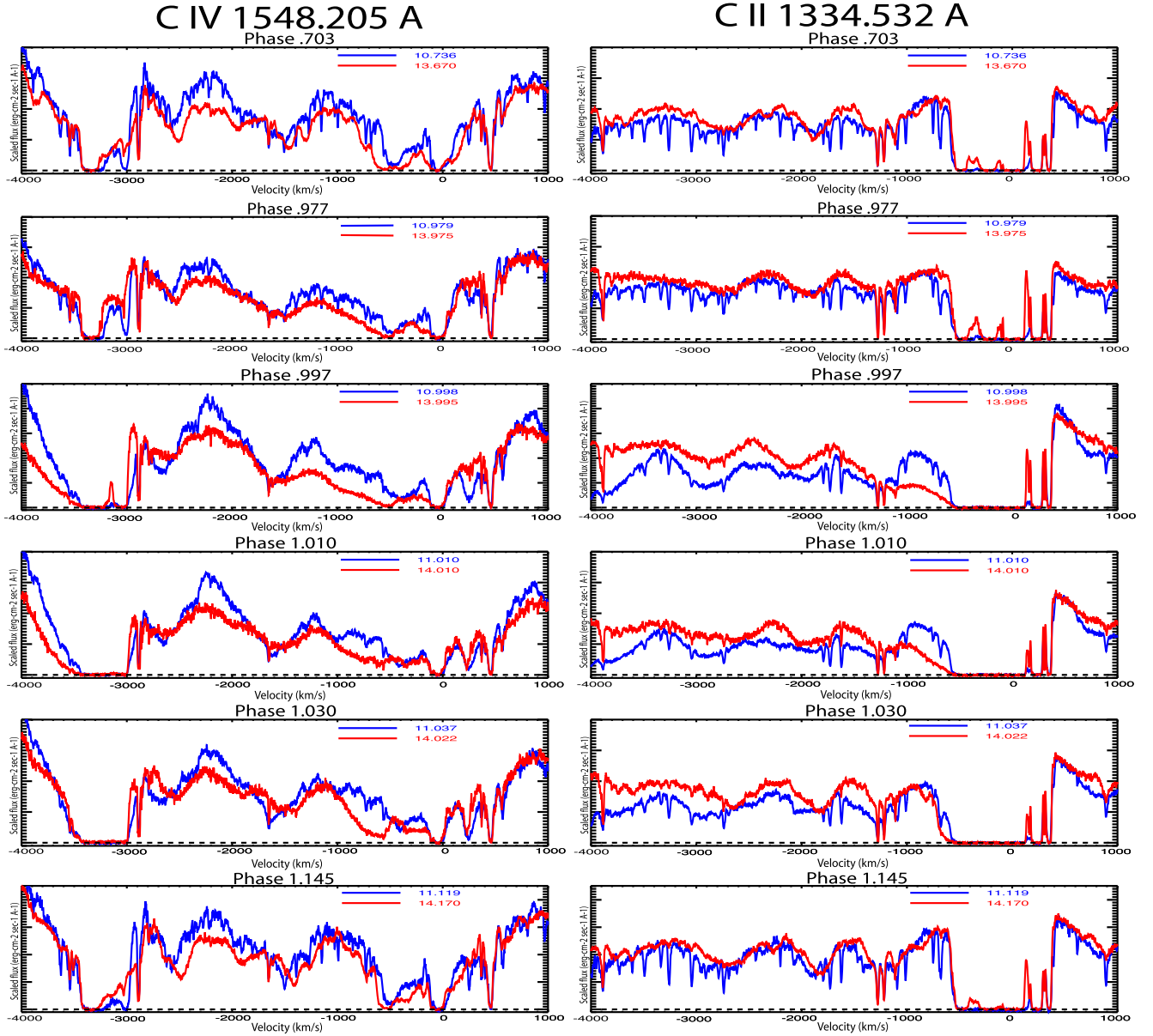


**Figure 10.** Comparison of C IV (IP = 47.9/64.5 eV) and C II (IP = 11.3/24.4 eV) profiles at six similar phases across cycles 10/11 (periastron passage 11) and 13/14 (periastron passage 14). Left column: The difference in C IV  $\lambda 1548$  absorption profiles indicates increased absorption from 0 to  $-2600 \text{ km s}^{-1}$  by cycle 13 compared to Cycle 10. Right column: C II  $\lambda 1335$  absorption profiles reveal a ramp-like absorption extending from  $-100$  to  $-600 \text{ km s}^{-1}$  across periastron passage 14 that was not present across periastron passage 11. Flux scaling was based on continuum levels from 1463 to  $1488 \text{ \AA}$ .

The normalized Si IV profiles (Figure 11) show no strong variations in absorption in the high-ionization phase either well before the periastron passage or in the early recovery to the high-ionization state. The absorption is nearly saturated from  $-100$  to  $-600 \text{ km s}^{-1}$ , especially for the  $\lambda 1394$  line, but continuum is present for the  $\lambda 1403$  line. Significant changes in the Si IV doublet lines do occur between the periastron passages cycles 11 & 14. Most notably, at  $\phi = 0.997$  absorption increased in the velocity range  $-1000 < v < -1600 \text{ km s}^{-1}$  in cycle 14 compared to cycle 11. Increased absorption in Si IV  $\lambda 1403$  continued throughout that velocity range across periastron passage 14.

The normalized Si II profiles (Figure 12) show stronger absorption in the range  $-100 < V < -400 \text{ km s}^{-1}$  for the  $\lambda 1533$  line compared to the  $\lambda 1527$  line, consistent with the *gf* values. Completely saturated absorption occurs from  $-400$  to

$-600 \text{ km s}^{-1}$  for both lines. A noticeable increase in absorption from  $-800$  to  $-1400 \text{ km s}^{-1}$  is present in the  $\lambda 1527$  line (and up to  $-1200 \text{ km s}^{-1}$  in the  $\lambda 1533$  line) in the high-ionization state across periastron passage 14 relative to periastron passage 11. Comparison of the  $\lambda 1527$  absorption profile to the CMFGEN model (Figure 8) indicates that the continuum in the high-ionization state approaches the model velocity profile in the  $-100$  to  $-400 \text{ km s}^{-1}$  interval. By cycle 14, the  $-170 \text{ km s}^{-1}$  absorption from the Little Homunculus disappeared across the high-ionization state because the increased FUV flux has caused most metal ions to become doubly ionized. Across the periastron passages, when the FUV flux of  $\eta \text{ Car B}$  is hidden as it passes behind the primary, the metals return to singly ionized states and absorption becomes nearly completely saturated from  $-100$  to  $-500 \text{ km s}^{-1}$  (Figure 12). However, weak continuum bumps are present at  $-100$  and  $-300 \text{ km s}^{-1}$  in both cycles at  $\phi = 0.997$ .



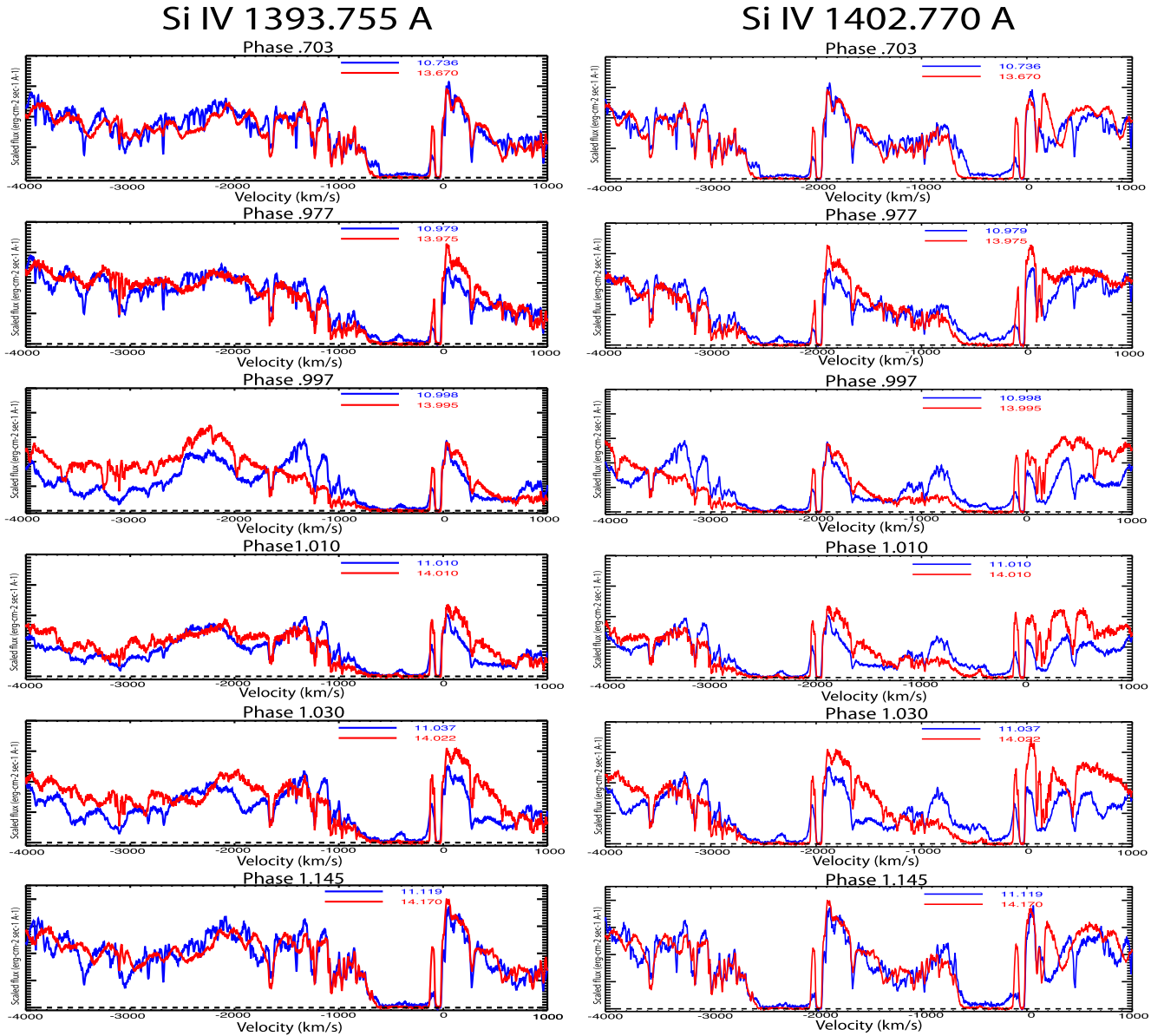


**Figure 11.** Comparison of Si IV (IP = 45.1 eV) at six similar phases across cycles 10/11 (periastron passage 11) and 13/14 (periastron passage 14). Although the Si IV lines show similar absorption profiles leading up to periastron passage, the absorption at  $\phi = 13.670$  extends further to the blue by about  $100 \text{ km s}^{-1}$ ; the difference is real because it is seen in both components. After periastron passage, the profiles are again very similar. The change in the “spike” near  $100 \text{ km s}^{-1}$  is likely due to changes in the circumstellar medium. Further examination shows that Si IV profiles during cycle 10 show a larger residual intensity in the absorption trough than during cycles 13/14. Significant differences between  $-1000$  and  $-2500 \text{ km s}^{-1}$  occur as periastron passage begins ( $\phi = 0.997$ )—the extended absorption is more obvious, is seen in both doublets, and appears to extend to velocities beyond  $-2000 \text{ km s}^{-1}$  in the cycle 13/14 data.

The  $\lambda 1533$  line is completely absorbed from  $-40$  to  $-500 \text{ km s}^{-1}$  at  $\phi = 1.010$  and  $1.030$ , but a spike of continuum survives at  $-100 \text{ km s}^{-1}$  for the  $\lambda 1527$  line. This indicates a gap in velocity between the slow-moving structure related to the Weigelt clumps (Gull et al. 2016) and the Little Homunculus.

#### 5.4.3. Comparing Al III and Al II Profiles

The Al III (IP = 18.8/28.5 eV) and Al II (IP = 6.0/18.8 eV) absorptions (Figure 13) probe the ionized gas above and below the ionization potential of hydrogen (IP = 13.6 eV), which is useful for probing the extended primary wind. However, the Al III is recorded by the E230M STIS grating, which unfortunately was not always used leading up to periastron passage 14. The three available profiles of Al III  $\lambda 1855$  show behavior similar to that of the Si IV doubles. The profiles in the  $\phi = 0.703$  spectrum and

$\phi = 1.145$  are quite similar for Al II and Al III. At  $\phi = 1.010$ , both lines show high-velocity absorption wings extending from  $-1000$  to  $-1300 \text{ km s}^{-1}$ , similar to the high-velocity absorption seen in the C and Si profiles. The profiles are nearly saturated in the  $-100$  to  $-600 \text{ km s}^{-1}$  range, but show less saturation in the  $-100$  to  $-400 \text{ km s}^{-1}$  range. The Al II  $\lambda 1671$  profiles show little variation in the high-ionization state,  $\phi = 0.703$  and  $0.933$ , but show increased absorption in the  $-100$  to  $-400 \text{ km s}^{-1}$  range from  $\phi = 0.977$  to  $1.030$ .

#### 5.5. Changes in Absorption Profiles across the Two Periastron Passages

The onset of periastron led to a plethora of changes in the STIS FUV spectrum across both periastron passages 11 and 14. From a broadband perspective, the flux declined 50%, based on

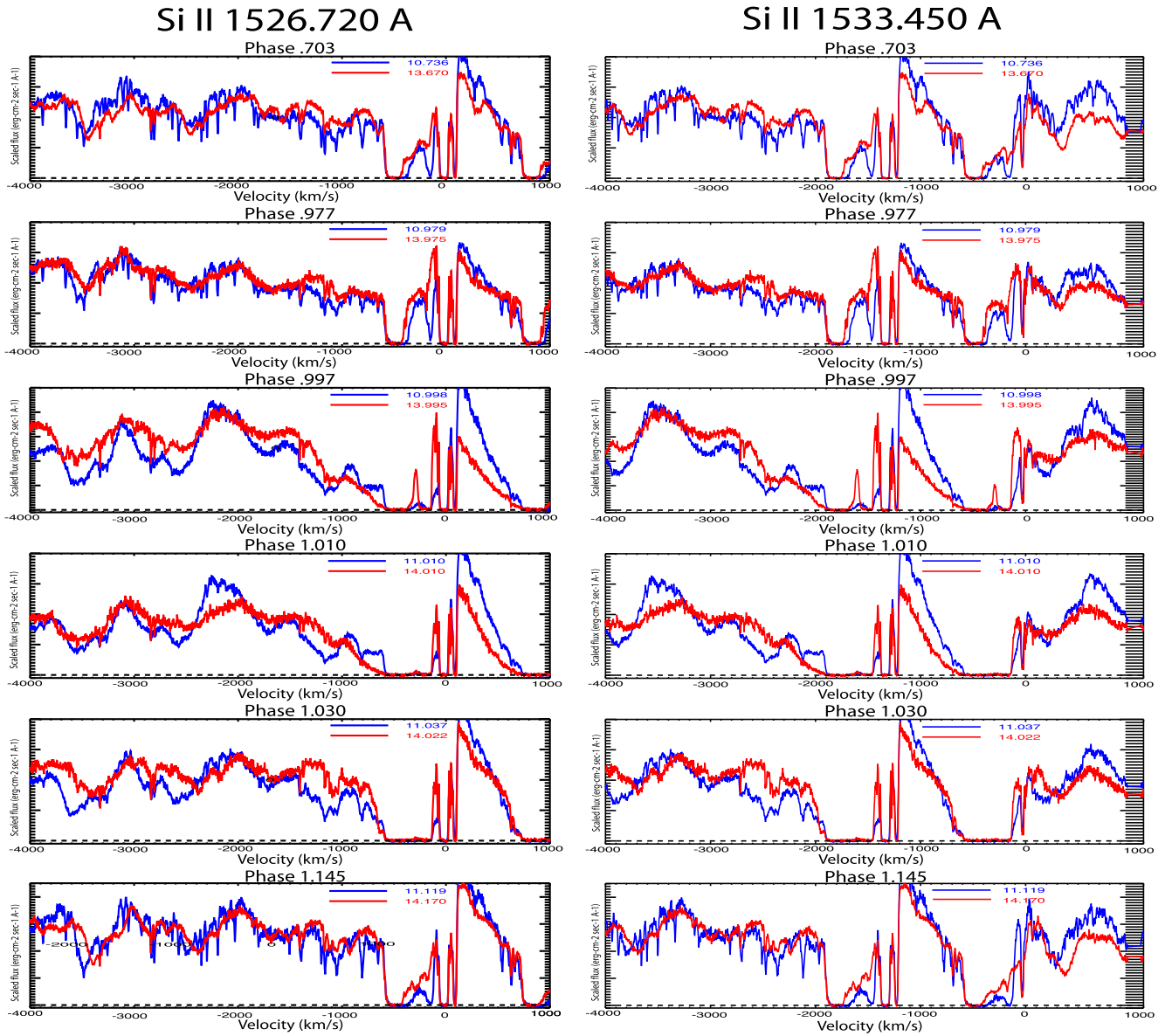


**Figure 12.** Comparison of Si II (IP = 8.2 eV) profiles at six similar phases across cycles 10/11 (periastron passage 11) and 13/14 (periastron passage 14). As for Si IV, the profiles outside of periastron passage are very similar, with differences most likely a consequence of blending. The biggest difference is the absence/weakness of the  $-146 \text{ km s}^{-1}$  component, which arises in the Little Homunculus, in the 13/14 cycle. During periastron passage, absorption has increased over  $-600$  to  $-1200 \text{ km s}^{-1}$ , with longer-wavelength absorption eating into the P Cygni emission component of the bluer member of the doublet.

the STIS global count rates, then recovered to pre-periastron levels. Most of the flux decline is caused by singly ionized species that become more prevalent along our line of sight due to a drop in ionizing flux near periastron passage when the shock cone around the companion points away from the foreground gas and the hot companion is buried in the inner wind of  $\eta$  Car-A. Considerable changes occur across both periastron passages. High-velocity changes in the resonant line profiles are stronger near periastron passage 14 compared to periastron passage 11. We do not know whether the observed variations were a continuous trend or part of an abrupt change in the system. However, visible-band ground-based monitoring observations show a continuous flux increase (Damineli et al. 2021), which suggests that the changes in the FUV are most likely part of this same continuous change.

Figures 14 to 16 compare profiles from well before periastron passage ( $\phi = 10.736$  and  $13.670$ ), early in the high-ionization

recovery ( $\phi = 11.119$  and  $14.170$ ), and near periastron passage ( $\phi = 11.010$  and  $\phi = 14.010$ ). Normalization was done using the “continuum” near  $1483 \text{ \AA}$  for most lines except for N V, which was normalized using continuum longward of  $1250 \text{ \AA}$ . Note, in reference to the N V velocity plots, that the monotonic increase in flux from  $-3500 \text{ km s}^{-1}$  conforms well to the wings of H I Ly $\alpha$ . As profiles for Al II and Al III for all three epochs came from E230M spectra, the profiles in Figure 16 were scaled to “continuum” near  $1800 \text{ \AA}$ .

### 5.5.1. Changes across Periastron Passage 11

Groh et al. (2010) previously compared high-velocity changes in seven resonant lines (excluding N V) leading up to periastron passage 11 (2003.5) to high-velocity changes in the He I  $\lambda 10830$  velocity profile leading up to the 2009.1 periastron. However, they did not discuss changes in the FUV

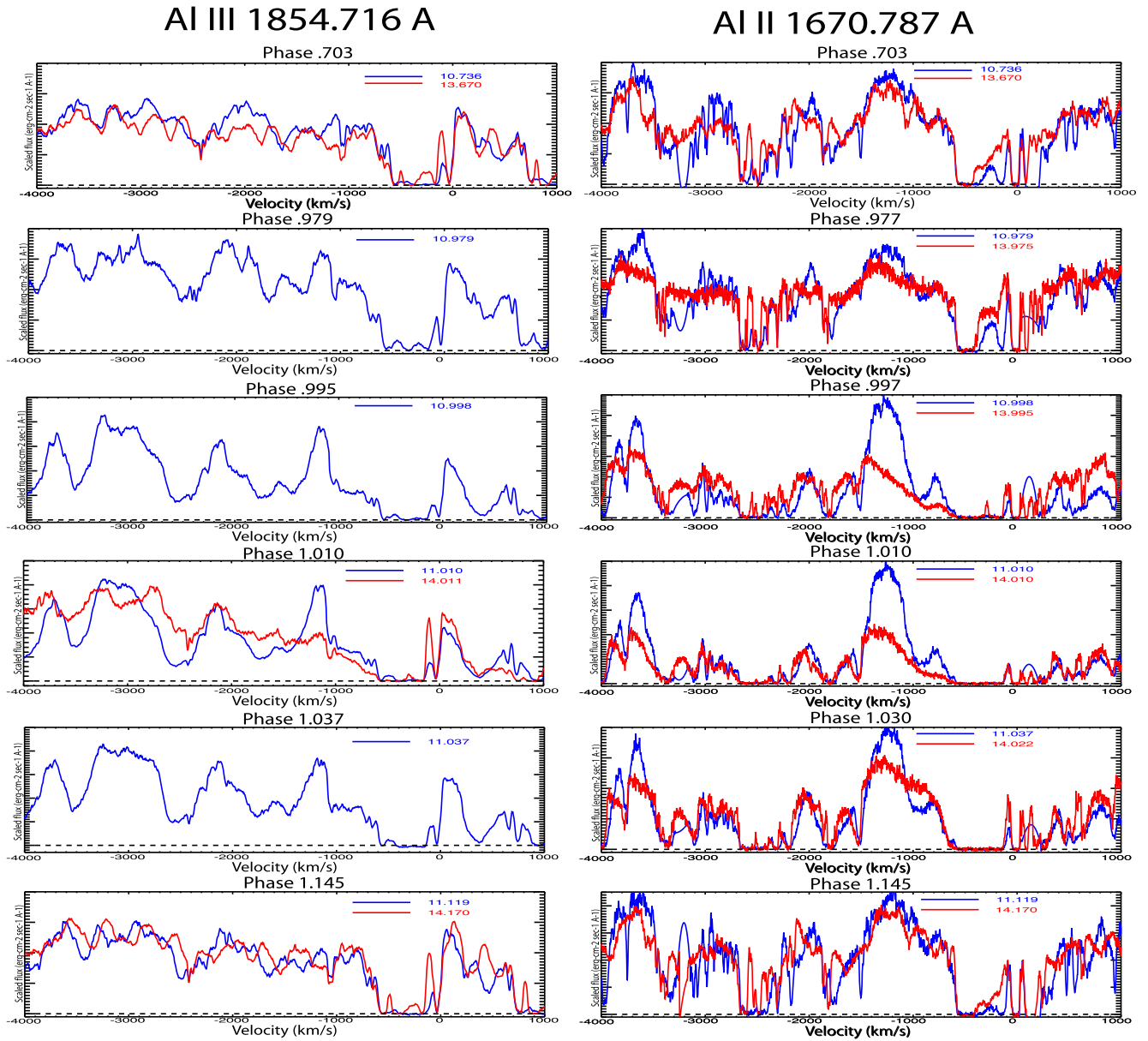


**Figure 13.** Comparison of Al III (IP = 18.8/28.5 eV) and Al II (IP = 6.0/18.8 eV) profiles at six similar phases across cycles 10/11 (periastron passage 11) and 13/14 (periastron passage 14). Left column: Only three comparison spectra are available for Al III  $\lambda 1855$  absorption profiles across cycles 10/11 (periastron passage 11) and 13/14 (periastron passage 14). Notable is the strong absorption in the  $-1000$  to  $-1300$  km s $^{-1}$  interval at  $\phi = 1.010$ . Right column: Al II  $\lambda 1671$  absorption profiles show minimal difference leading up to and after the periastron passages. As with all low-ionization lines, a ramp-like absorption appears from  $-600$  to  $-400$  km s $^{-1}$  across periastron passage 14. Both the Al III and Al II profiles were normalized to the continuum near  $1800$  Å. Note that the flux is invalid for Al II from  $+100$  to  $+400$  km s $^{-1}$ , due to echelle format dropout.

near periastron passage 11. Here, we compare profiles before, during, and after the periastron passages 11 and 14 from  $-4000 < V < +1000$  km s $^{-1}$ , with particular focus on changes near the periastron passage.

Profiles are plotted in velocity space for eight resonant lines in Figures 14 through 16 (left columns) for three selected phases: high-ionization state before periastron passage ( $\phi = 10.736$ ), low-ionization state deep in periastron passage ( $\phi = 11.010$ ), and early recovery to high-ionization state ( $\phi = 11.119$ ). This comparison shows that changes in the NV profile are dominated by other absorptions at  $\phi = 11.010$  (Figure 14, lower left). The CIV absorption increased in the  $-700$  to  $-1200$  km s $^{-1}$  range and possibly in the range from  $-1500$  to  $-1800$  km s $^{-1}$  (Figure 14, middle two left), but the CIV absorption in the  $-100$  to  $-600$  km s $^{-1}$  range is obscured

by iron absorptions as shown in Section 5.3 and Figure 8. Changes in the two Si IV velocity profiles appear inconsistent because they are heavily modulated by lower-ionization absorptions across periastron 11 (Figure 15, lower left two panels). Increased absorption may be present from  $-1300$  to  $-2200$  km s $^{-1}$ . The C II velocity profile (Figure 14, upper left) also appears to be modulated by other absorption lines at velocities more negative than  $-600$  km s $^{-1}$ . On the other hand, the two Si II profiles do not appear to be modulated by other absorption lines (Figure 15, upper left two panels). The Al II velocity profile (Figure 16) shows an increase in absorption from  $-600$  to  $-1200$  km s $^{-1}$  near periastron passage (Figure 16, upper left), while the two Al III profiles show similar absorptions from  $-600$  to  $-1200$  km s $^{-1}$  (Figure 16, lower left two panels). The apparent absorptions extending above  $-3000$  km s $^{-1}$  in

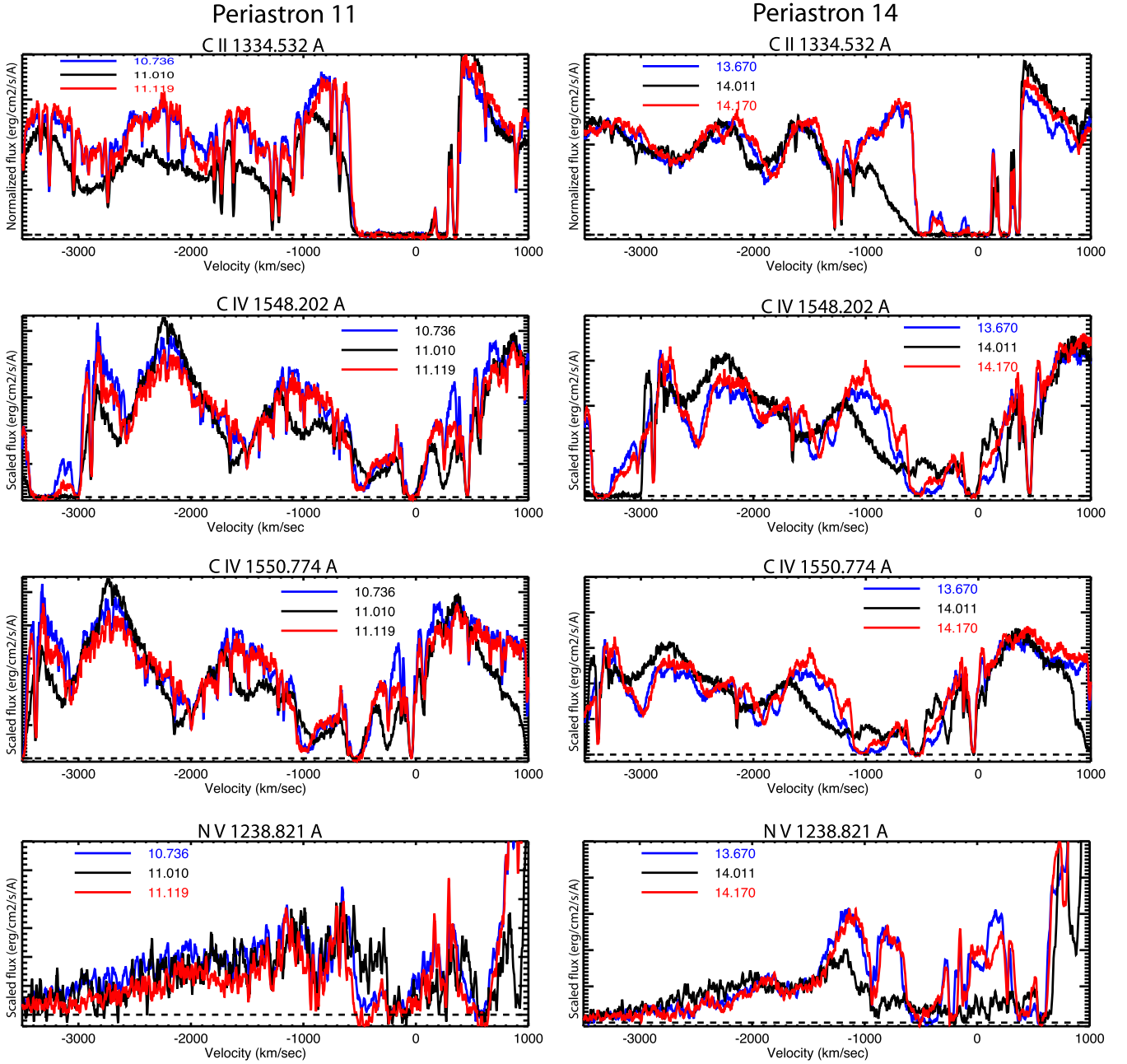


**Figure 14.** Variations of profiles across periastrons 11 (left column) and 14 (right column). Top row: C II  $\lambda 1335$ . Middle rows: C IV  $\lambda\lambda 1548, 1551$ . Bottom row: N V  $\lambda 1239$ . The most noticeable difference is the ramp-like absorption from  $-500$  to  $-1200$  km s $^{-1}$  in the C II and C IV profiles during periastron passage 14. The C II absorption, which shows islands of lower absorption before and after periastron passage 14, becomes completely saturated during periastron passage 14. While strong variations occur in the C IV  $\lambda 1551$  velocity profile from  $-100$  to  $-3000$  km s $^{-1}$ , the narrow absorption centered on  $-40$  km s $^{-1}$  does not change. (C II (doublet separation equivalent to 284 km s $^{-1}$ ), C IV (separation 498 km s $^{-1}$ ), and N V (915 km s $^{-1}$ ) overlap so closely that complete isolation of doublet contributions is not possible.)

Al III  $\lambda 1855$  are likely contributions from weaker absorbing lines. The Si II and Al II absorptions saturate from  $-100$  to  $-400$  km s $^{-1}$  at  $\phi = 11.010$  (Figure 15, upper left two panels, and Figure 16, upper left panel).

### 5.5.2. Changes across Periastron Passage 14

Many noticeable changes occur with the apparent brightening of  $\eta$  Car by periastron passage 14. Velocity profiles of the same eight resonant lines are plotted in Figure 14 through 16 (right columns) for three selected phases: high-ionization state before periastron passage ( $\phi = 13.670$ ), low-ionization state

deep in periastron passage ( $\phi = 14.010$ ), and early recovery to high-ionization state ( $\phi = 14.170$ ). We see that all resonant line profiles experienced increased absorptions across the interval from  $-600$  to at least  $-1200$  km s $^{-1}$  (Figures 14 through 16, right columns). The N V resonant line absorption across  $-600$  to  $-1400$  km s $^{-1}$  increased in absorption from  $\phi = 13.670$  to  $\phi = 14.011$ , then a peak in emission appears by  $\phi = 14.170$ . The C IV absorptions at  $\phi = 14.011$  decreased continuously from  $-300$  km s $^{-1}$  to  $-500$  km s $^{-1}$  relative to the profiles measured at  $\phi = 13.886$  and  $\phi = 14.170$  (Figure 14, right middle two panels). At  $\phi = 14.010$ , the C IV absorption has dropped, revealing the iron-dominated velocity profile of



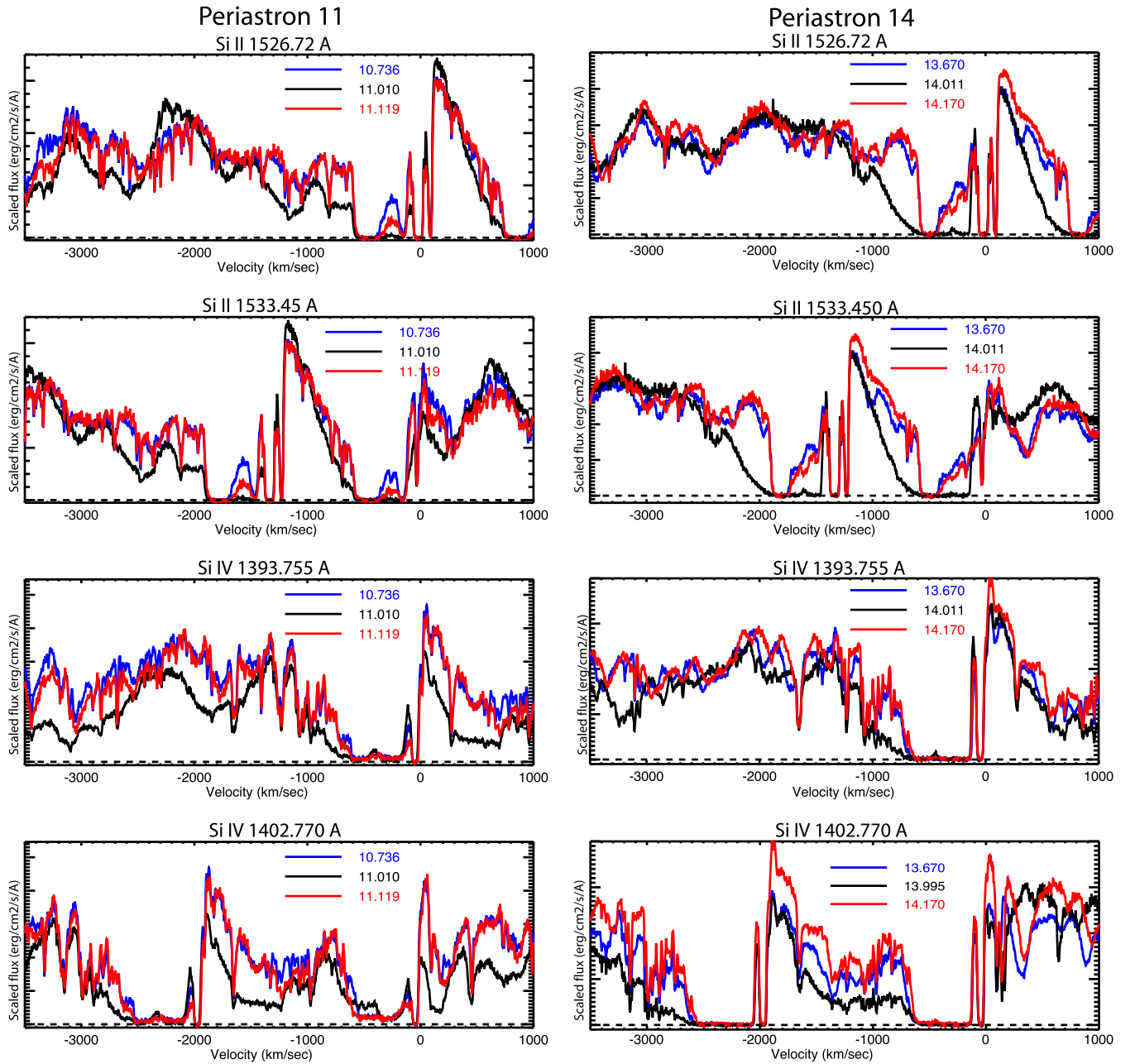


**Figure 15.** Comparison of profiles across periastrons 11 (left column) and 14 (right column). Top two rows: Si II  $\lambda\lambda$  1527, 1533. The Si II  $\lambda$ 1527 and possibly the Si II  $\lambda$ 1533 appear to have two components of absorption between  $-500$  to  $-700$  km s $^{-1}$  and  $-1000$  to  $-1300$  km s $^{-1}$  across periastron 11, while both Si II lines show a very smooth absorption ramp from  $-500$  to  $-1000$  km s $^{-1}$  across periastron passage 14. Two islands of lesser absorption are present before and after periastron passage 11, centered on  $-100$  and  $-300$  km s $^{-1}$ , that disappear across periastron passage 11. The lesser absorption extends from  $-100$  to  $-350$  km s $^{-1}$  before and after periastron passage 14, but disappears across the passage. Bottom two rows: Si IV  $\lambda\lambda$  1394, 1403. The Si IV profiles are affected by other absorption lines. Across periastron passage 11, the  $-100$  to  $-600$  km s $^{-1}$  region is not completely saturated, indicating a drop in FUV ionizing flux, but the profiles are quite similar both before and after periastron passage. The Si IV  $\lambda$ 1403 shows an increased saturation from  $-1300$  to  $-1900$  km s $^{-1}$ . Across periastron passage 14, the  $-100$  to  $-600$  km s $^{-1}$  velocity interval is completely saturated.

$\eta$  Car-A (see Figure 8). The two Si IV resonant lines increased in absorption from  $-700$  and  $-1800$  km s $^{-1}$  by  $\phi = 14.011$  relative to  $\phi = 13.667$ . Both profiles then decreased in absorption by  $\phi = 14.170$ . Neither the C IV nor the NV profiles are saturated in the  $0$  to  $-600$  km s $^{-1}$  range, indicating that most of the primary wind is in a lower-ionization state. All four singly ionized (Al II, C II, and Si II  $\lambda\lambda$  1527, 1533) profiles reveal very strong increased absorption extending from  $-600$  to  $-1500$  km s $^{-1}$  by  $\phi = 14.011$ , relative to profiles measured at  $\phi = 13.670$ , and return nearly to the pre-periastron profiles

by  $\phi = 14.011$ . The resonant absorptions, extending from  $-100$  to  $-420$  km s $^{-1}$  of Si II and Al II, saturate by  $\phi = 14.011$ , indicating absorbers most likely in the Homunculus and Little Homunculus relaxed from higher-ionization states to singly ionized states, but returned to the high-ionization state by  $\phi = 14.170$ . This absorption was stronger across periastron passage 14 than across 11.

The most prominent changes are the nearly linear absorption profiles ranging from  $-600$  to  $-1500$  km s $^{-1}$  present in NV through Al II. This structure was noted by Gull et al. (2021) in

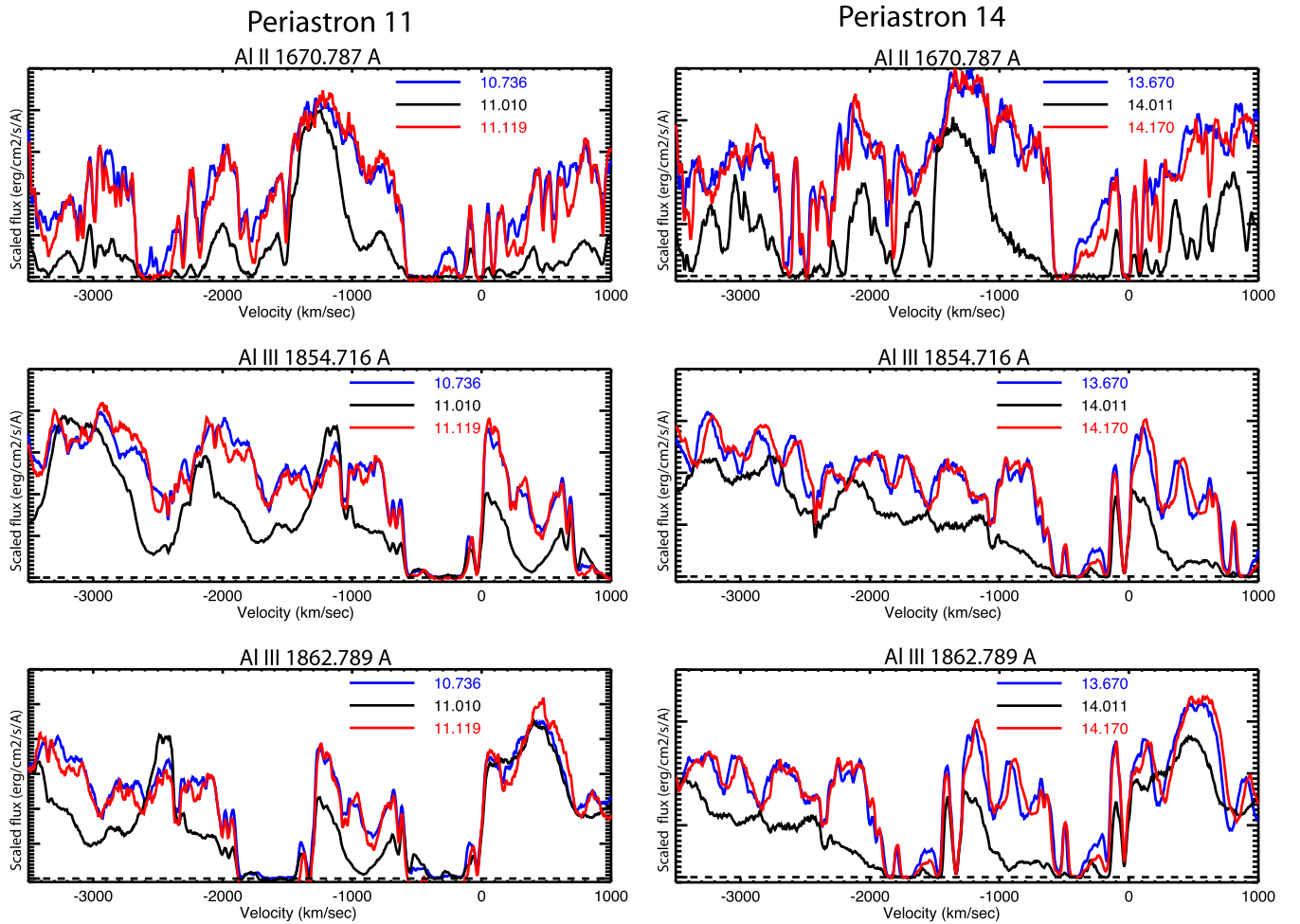


**Figure 16.** Comparison of Al II and Al III profiles across periastron passages 11 (left column) and 14 (right column). Top row: Al II  $\lambda 1671$ . Before and after periastron passage, they are virtually identical. Across periastron passage 14, the ramp-like absorption extends from  $-60$  to  $-1400$  km s $^{-1}$  and the  $-100$  to  $-400$  km s $^{-1}$  region became saturated. Bottom two rows: Al III  $\lambda\lambda 1855, 1863$  profiles. The Al III  $\lambda 1855$  indicates possible continuous ramp absorption from  $-600$  to  $-2200$  km s $^{-1}$  across periastron passage 14, but only to  $-1100$  km s $^{-1}$  across periastron passage 11.

singly ionized absorption profiles. It is likely that the transient absorption is the velocity-dispersed structure of the WWC trailing arm (Madura et al. 2012, 2013).

### 5.5.3. Comparison of Doublet Profiles

Comparison of doublet profiles provides a critical test of the identification of velocity components of the resonant lines, as we noted in Section 5.2. The doublet velocity comparison provides discrimination against absorptions from other lines. We apply this test to the same three spectra discussed in Section 5.5.1 and 5.5.2 to parse changes between the high-ionization and low-ionization states, especially across the periastron passages (Figures 17 through 21). The doublet velocity profile comparisons are not continuum-normalized, since the profiles are from the same spectrum.

The NV  $\lambda\lambda 1238, 1243$  profiles were difficult to isolate (Figure 17). The increased density of absorbing lines below  $1300\text{\AA}$  and the wings of the strong, extremely saturated H I Ly $\alpha$  profile depresses the continuum across the NV velocity profile. The profiles presented in Figure 17 are smoothed to  $20$  km s $^{-1}$  resolution in order to improve the signal-to-noise ratio. The doublet profiles overlap in the high-ionization state before and after both periastron passages, but no evidence of NV absorption is present close to periastron passage. This

suggests that  $\eta$ Car-B is the source of the ionization flux that producing N $^{+4}$  (IP =  $77.5$  eV). NV disappears when the ionizing flux from  $\eta$ Car-B is totally absorbed by the extended wind of  $\eta$ Car-A across periastron passage.

Before and after periastron passage 11, the NV absorption is centered at  $-400$  km s $^{-1}$  (Figure 17, top row). The absorption width at  $\phi = 10.818$  appears to increase from  $250$  km s $^{-1}$  before passage to  $400$  km s $^{-1}$  post-passage. Before and after periastron passage 14, the NV absorption is centered at  $-450$  km s $^{-1}$  but does not appear to change significantly from  $300$  km s $^{-1}$  in width (Figure 17, bottom row). The blueward absorption wing may be present in NV up to  $-1000$  km s $^{-1}$  at  $\phi = 13.995$ , similar to the high-velocity absorption wing that extends from  $-600$  to  $-1400$  km s $^{-1}$  in profiles from less-ionized lines, as noted above.

The C IV  $\lambda\lambda 1548, 1552$  doublet (IP =  $47.9$  eV) is likewise complex, due to confusing absorptions from the iron spectrum of  $\eta$ Car-A. The velocity overlap of the doublets is not completely consistent before, during, and after periastron passage 11 (Figure 18, top row) as seen across periastron passage 14 (Figure 18, bottom row). Examination of the CMFGEN model profile (Figure 8, top right) indicates that this portion of the  $\eta$ Car-A spectrum is dominated by iron absorptions. The velocity profile of C IV  $\lambda 1548$  at  $\phi = 10.998$

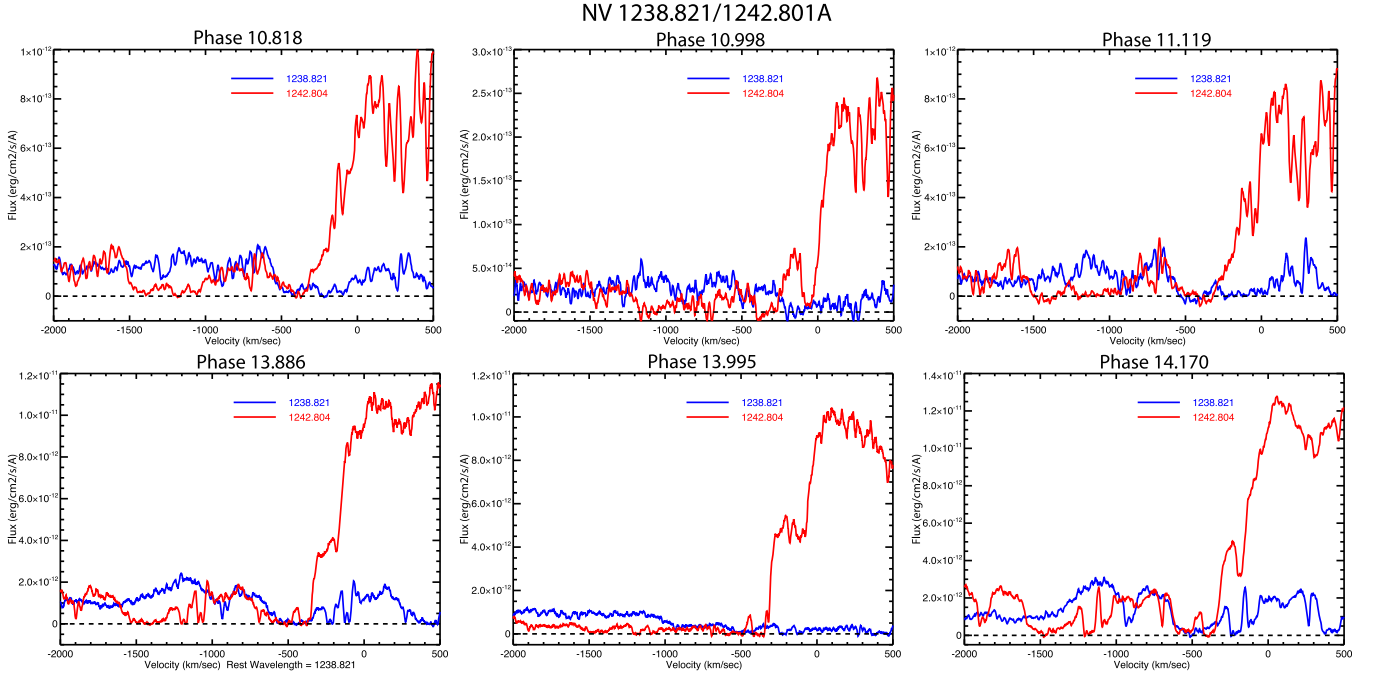


**Figure 17.** Velocity profiles of N V  $\lambda$ 1239,1243 doublet (IP + 77.5 eV). The velocity comparison shows a broad absorption before and after, but not during, both periastron passages. Top row: For periastron passage 11, the  $\approx 300 \text{ km s}^{-1}$ -wide absorption is centered at  $-400 \text{ km s}^{-1}$ . Bottom row: For periastron 14, the absorption has widened to  $\approx 400 \text{ km s}^{-1}$  and shifted to  $-500 \text{ km s}^{-1}$ . The shorter wavelength is plotted in blue. The longer wavelength is plotted in red.

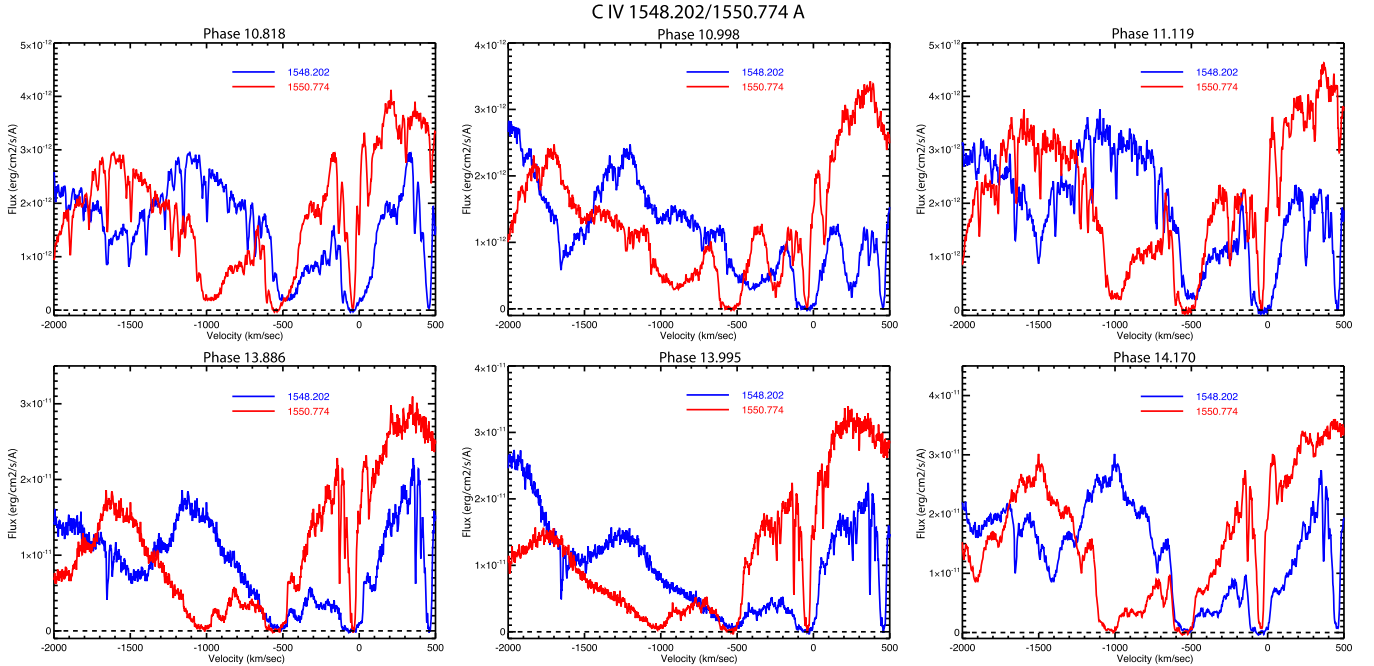


**Figure 18.** Velocity profiles of the C IV  $\lambda$ 1548,1551 doublet (IP = 47.9 eV). Top row: Reinforcement of profiles is limited. Before and after periastron passage 11, the velocity components appear to have been shifted in velocity but are confused by absorption from an iron line. The likely component is centered near  $-500 \text{ km s}^{-1}$  and is a few hundred  $\text{km s}^{-1}$  wide. Across periastron 11 ( $\phi = 10.998$ ), the profiles are dominated by iron lines with no C IV absorption present. Bottom row: A common absorption component before and after periastron passage 14 is centered at  $-550 \text{ km s}^{-1}$  with  $200 \text{ km s}^{-1}$  width, and remains across periastron 14 ( $\phi = 13.995$ ) along with an absorption ramp that extends well beyond  $-800 \text{ km s}^{-1}$ . The shorter wavelength is plotted in blue. The longer wavelength is plotted in red.

(Figure 18, top row, center) is quite similar to the absorbed profile generated by the CMFGEN model. Iron absorption leads to the less consistent overlap of the C IV profiles even in the high-ionization state before and after periastron passage 11. The C IV velocity profile in the high-ionization state appears to be unsaturated, centered at  $-450 \text{ km s}^{-1}$ , and have a width of  $\sim 100 \text{ km s}^{-1}$ . In contrast, the profiles of the C IV doublet are

consistent across periastron passage 14 (Figure 18, bottom row), most likely because of the greatly increased contribution in flux from the central core of  $\eta$  Car-A that led to a deeper, more direct view of the interacting wind structures in our LOS. The C IV profiles are centered at  $-550 \text{ km s}^{-1}$ , and saturated with a width of a few hundred  $\text{km s}^{-1}$ . Comparison of variations in the C IV profiles across the two periastron

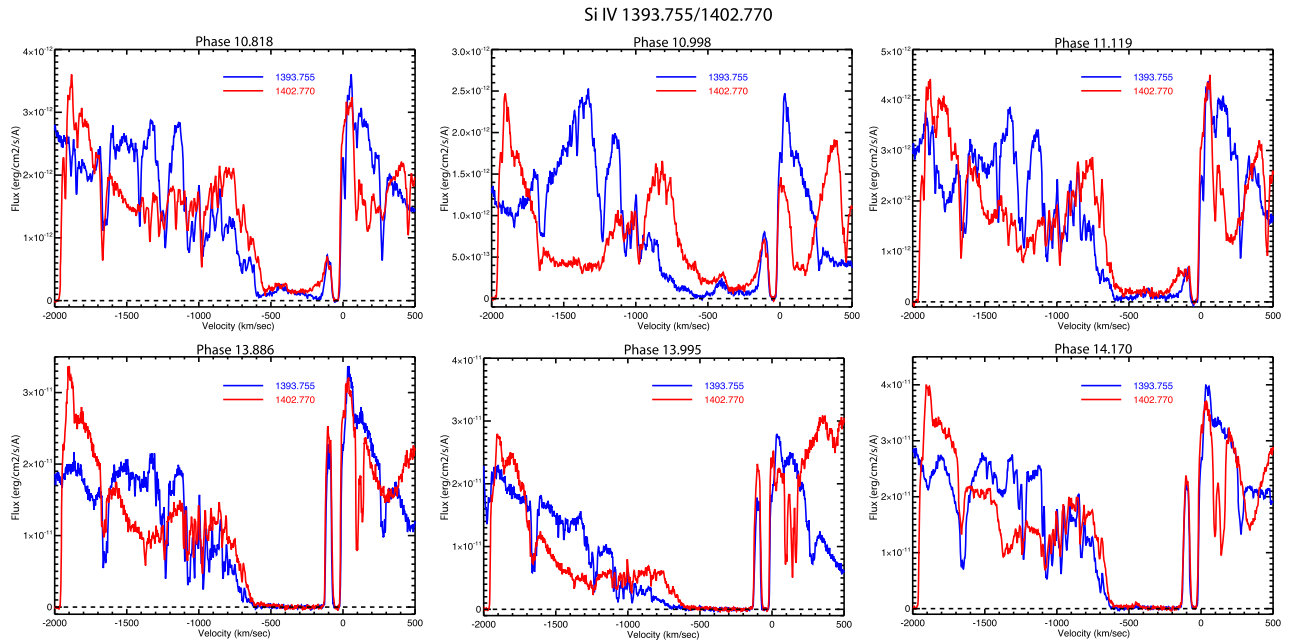


**Figure 19.** Velocity profiles of the Si IV  $\lambda\lambda$  1394,1403 doublet ( $IP = 33.5$  eV). Top row: The  $-100$  to  $-600$   $\text{km s}^{-1}$  absorption, while strong, is not saturated throughout periastron passage 11. A strong absorption appears across periastron, extending from  $-400$  to  $-1000$   $\text{km s}^{-1}$ . Bottom row: The  $-100$  to  $-600$   $\text{km s}^{-1}$  velocity range is completely saturated before, during, and after periastron passage 14. However, the high-velocity profile does not track closely before and after the periastron passages. The shorter wavelength is plotted in blue. The longer wavelength is plotted in red.

passages reinforces the importance of the iron spectrum on this spectral interval. All profiles associated with periastron passage 11 show the influence of the iron spectrum in the  $0$  to  $-600$   $\text{km s}^{-1}$  interval (see Figure 9). That contribution is less apparent and reinforces the hypothesis that originally a small amount of FUV continuum from the core of  $\eta$  Car-A passed through the occulter in our LOS.

The Si IV  $\lambda\lambda$  1394,1403 doublet is far more consistent than either the NV or CIV doublets, likely because of its lower ionization energy ( $IP = 33.5$  eV). It characterizes structure more distant than the immediate WWC, which produces the NV and CIV absorptions, where the ionizing flux has dropped in energy to well below the IP of  $\text{C}^{+3}$  (64.5 eV). The velocity overlaps are much better defined for both periastron passages (Figure 19).

None of the Si IV profiles near periastron passage 11 reach saturation even across the  $-100$  to  $-600$   $\text{km s}^{-1}$  range. This indicates that the LOS views of the interacting winds and shell structures are not completely ionized. Some decrease in absorption is notable at  $\phi = 10.998$  compared to just before and just after periastron passage ( $\phi = 10.818$  and  $11.119$ ). In contrast, that entire velocity range is saturated for all profiles associated with periastron passage 14. Along the LOS from the continuum-emitting core of  $\eta$  Car-A through the winds and the expanding shells, the continuum flux is entirely absorbed even deep in the low-ionization state induced by the periastron passage.

The Al III  $\lambda\lambda$  1855,1863 doublet behaves very consistently across both periastron passages (Figure 20).  $\text{Al}^{+2}$  has an  $IP = 18.83$  eV, well above the IP of hydrogen ( $IP = 13.6$  eV), while  $\text{Al}^{+}$  has an  $IP = 5.99$  eV. Changes in absorption by Al III provide a reference for the ionization levels of the extended wind of  $\eta$  Car-A, the very cool wind–wind collision zones, and the discrete absorbing shells within the Homunculus.

The Al III absorption profiles associated with periastron passage 11 (Figure 20, top row) show only small changes

between  $-100$  and  $-600$   $\text{km s}^{-1}$ , which indicates very little change in the ionizing flux at  $18.8$  eV. In contrast, across periastron 14 (Figure 20, bottom row), significant changes occur in the low-ionization state ( $\phi = 13.995$ ) compared to phases before and after periastron passage. The absorption increased during the low-ionization state, indicating that substantial amounts of aluminum must be in the high-ionization state,  $\text{Al}^{+3}$ , which requires a source of  $>28.45$  eV radiation. The Al III profiles do not produce an as-well-defined strong component around  $-500$   $\text{km s}^{-1}$  as do other resonant lines discussed in this paper.

The Si II  $\lambda\lambda$  1527,1533 doublet shows the most variable changes before, during, and after periastron passages (Figure 21). Yet both doublet profiles track each other remarkably well. The Si II absorption greatly increases across the low-ionization state, but the Si IV absorption remains saturated, indicating that much silicon is doubly ionized in the high-ionization state.

All high-ionization state profiles show a strong absorption component near  $-500$   $\text{km s}^{-1}$ . Before and after periastron passage 11, profiles (Figure 21, top column, left and right panels) show strong, saturated absorption centered at  $-475$   $\text{km s}^{-1}$ , with a  $200$   $\text{km s}^{-1}$  width. Before and after periastron 14, profiles show a similar profile, centered at  $-500$   $\text{km s}^{-1}$ , saturated but narrower, with a  $<200$   $\text{km s}^{-1}$  width. Al III is the exception, as it shows a saturated absorption at  $-600$   $\text{km s}^{-1}$  even across periastron passage 14.

The  $-100$  to  $-600$   $\text{km s}^{-1}$  velocity interval is strongly affected across the periastron passages but in very different ways in cycle 11 and 14. Before, during, and after periastron passage 11, a strong, relatively narrow, absorption centered at  $-150$   $\text{km s}^{-1}$  cuts the continuum, modulated by the apparent P Cygni velocity profile, which persists to about  $-300$   $\text{km s}^{-1}$  and then drops to the strong absorption previously mentioned at  $-475$   $\text{km s}^{-1}$ . Very close to periastron passage ( $\phi = 11.010$ ), absorption becomes saturated, except for weak emission



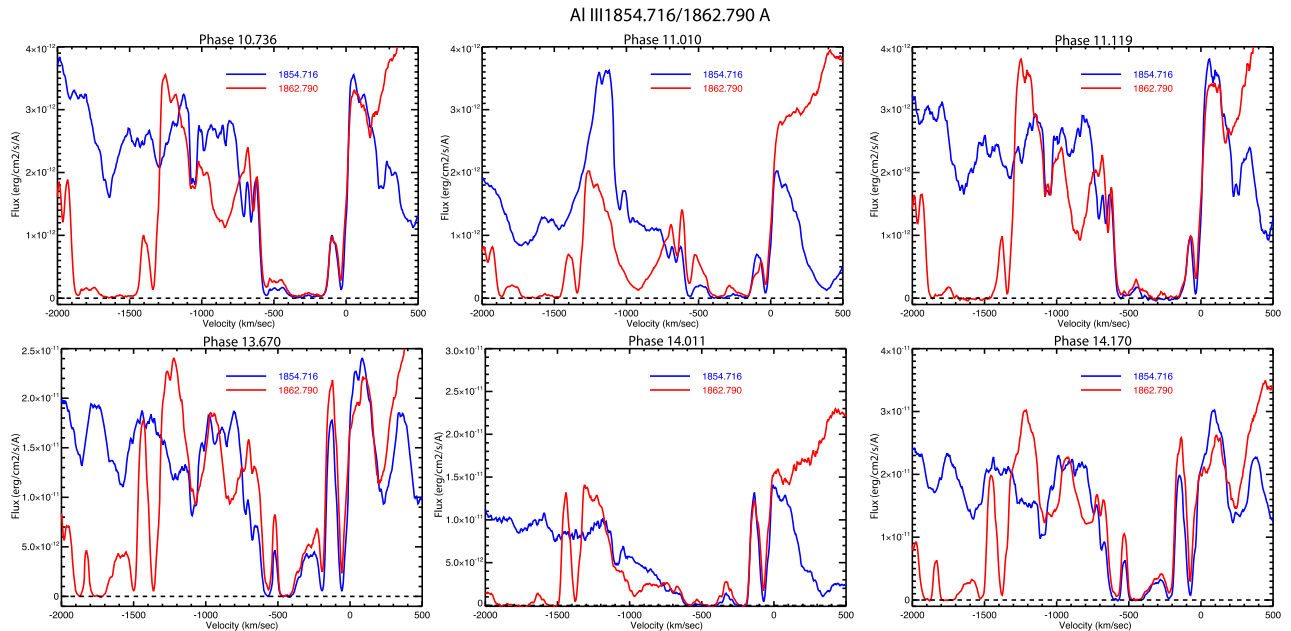


**Figure 20.** Velocity profiles of the Al III  $\lambda\lambda$  1855,1863 doublet (IP = 28.5 eV). Top row: Across periastron 11 ( $\phi = 11.010$ ), the  $-600$  to  $-1200$  km s $^{-1}$  absorption increases. Bottom row: The weak absorption islands at  $-100$  and  $-300$  km s $^{-1}$  strengthen across periastron passage 14 ( $\phi = 14.011$ ) but return to pre-passage levels afterward. The Al III velocity profile was not available at  $\phi = 13.995$ . The shorter wavelength is plotted in blue. The longer wavelength is plotted in red.

between  $-200$  and  $-300$  km s $^{-1}$ . By the early recovery to the high-ionization state ( $\phi = 11.119$ ), the absorption has partially decreased between  $-200$  to  $-300$  km s $^{-1}$ . In contrast, before periastron passage 14 ( $\phi = 13.886$ ), the P Cygni profile is recognizable to  $-350$  km s $^{-1}$ , especially for Si II and Ni II absorptions, and the  $-150$  km s $^{-1}$  component is nearly absent. During the low-ionization state near periastron 14, the P Cygni profile is nearly gone, as two saturated velocity components arise:  $-100$  to  $-250$  km s $^{-1}$  and  $-325$  to  $-600$  km s $^{-1}$ . By  $\phi = 14.170$ , the continuum has only partially recovered to the level seen in the P Cygni profile before periastron passage 14.

## 6. Discussion

In this paper, we have made a detailed investigation into UV line profiles as a function of cycle and orbital phase. While profile variations with orbital phase are linked with the highly eccentric orbit, the variations between cycles 11 and 14 are most likely due to the disappearance of the occulter—and not to an intrinsic variation in either of the stars.

Previously, Davidson et al. (2018) suggested that the brightening of  $\eta$  Car is caused by a decrease in the mass-loss rate of  $\eta$  Car-A. However, the X-ray light curve over the past five binary periods does not support such a claim, as fluxes clocked by orbital phase have not changed appreciably (except for a brief interval near the end of the X-ray minimum). In particular, the X-ray flux measured at apastron is effectively the same from orbit to orbit, as is the rise of the light curve into periastron passage (Espinoza Galeas 2021; Espinoza Galeas 2022, accepted). Recovery of the post-periastron X-ray flux does vary from passage to passage, but is thought to be governed by instabilities of the WWC in early recovery (Corcoran et al. 2017). Pittard (2007) pointed out that 3D hydrodynamic models of wind–wind shocked regions tend to smooth and dissipate clumps as they enter the shocked structures. Hence, once the WWC zone has stabilized,

variations across the extended high-ionization state would be minimal.

The systematic decrease in line equivalent widths (e.g., H $\alpha$ , Fe II) over the last decade could also be interpreted as evidence for stellar variability (Mehner et al. 2012, 2015). However, Daminieli et al. (2021) showed that the decreases could be better explained by the dissipation of the occulter. H $\alpha$ , Fe II, and [Fe II] lines originate in the outer region of the wind, and were less affected by the occulter. As the occulter dissipated (and/or moved out of the LOS), the EW would decline due to the rise in continuum flux. The existence of the occulter also explains why the models of Hillier et al. (2006) underestimated the strength of H $\alpha$ , and why H $\alpha$  EWs are lower when measured in spectra reflected from the lobes. The dissipating occulter now allows one to get a much better view of the WWC zone and spectral changes near periastron.

We found further evidence for transient, high-velocity absorption wings seen in profiles near periastron 14, in Si II (Gull et al. 2021) and other singly ionized resonant lines extending across a range of ionization potential from 6 eV (Al II) to 64.5 eV (C IV) (see Figures 10 to 13). This high-velocity absorption wing occurs contemporaneously when the X-ray flux begins to drop, as the WWC possibly collapses for a short interval near periastron passage (Hamaguchi et al. 2007; Madura et al. 2013; Clementel et al. 2015).

The downstream bow shock is the source of the  $-500$  km s $^{-1}$  absorption seen in the resonant lines from Al II to N V. The primary wind that flowed for at least several weeks in our LOS across the periastron passage (extending from the trailing arm of the old WWC to the leading arm of the new WWC) is shocked and accelerated by the secondary wind. Evidence of ionization and acceleration of this primary wind by the secondary wind is seen directly by the transient high-velocity absorption wing near periastron passage. The STIS FUV observations across periastron 14 show that this high-velocity absorption appeared by  $\phi = 13.995$  and persisted to  $\phi = 14.011$  (about 33 days). The wing is not present at

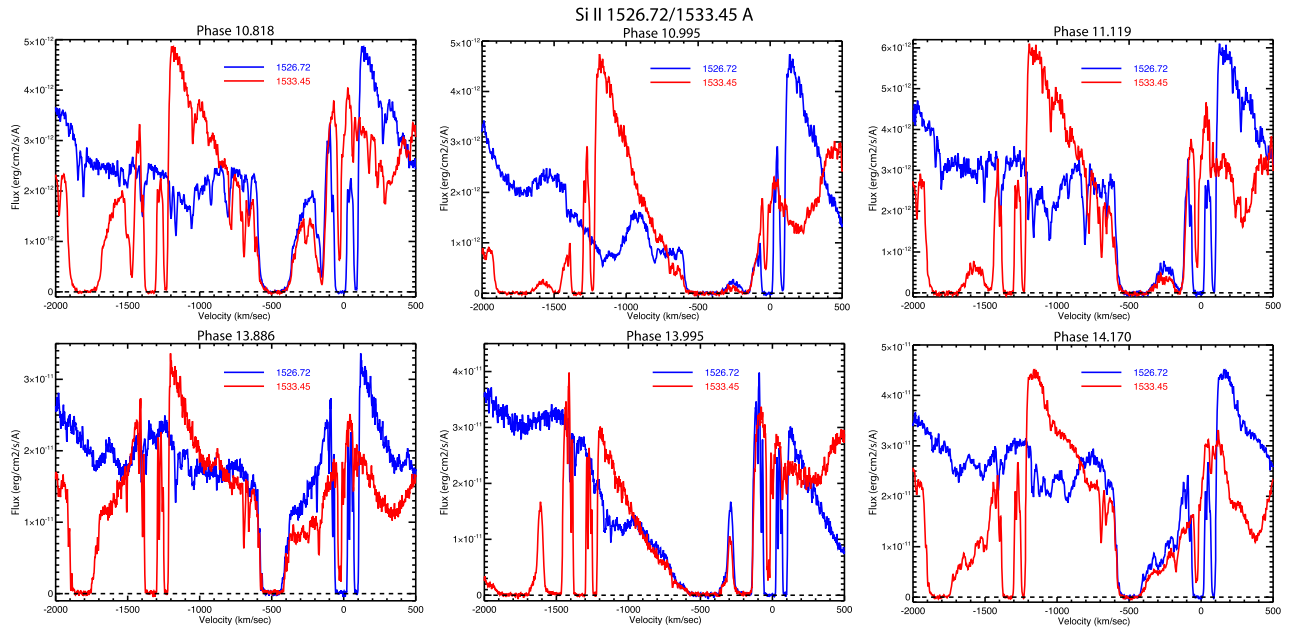


**Figure 21.** Velocity profiles of the Si II  $\lambda\lambda$  1527,1533 doublet (IP = 8.2 eV). Top row: Absorption from  $-100$  to  $-350$  km s $^{-1}$  is weak before, strengthens during, and partially recovers after periastron passage 11. Bottom row: Even weaker absorption is continuous from  $-100$  to  $-400$  km s $^{-1}$  but saturated from  $-400$  to  $-600$  km s $^{-1}$  before periastron. The ramp absorption occurs across periastron passage 14 ( $\phi = 13.995$ ) and disappears after periastron passage ( $\phi = 14.170$ ). The saturated absorption, while still centered close to  $-500$  km s $^{-1}$  is narrower in width across periastron passage from 13 to 14. The shorter wavelength is plotted in blue. The longer wavelength is plotted in red.

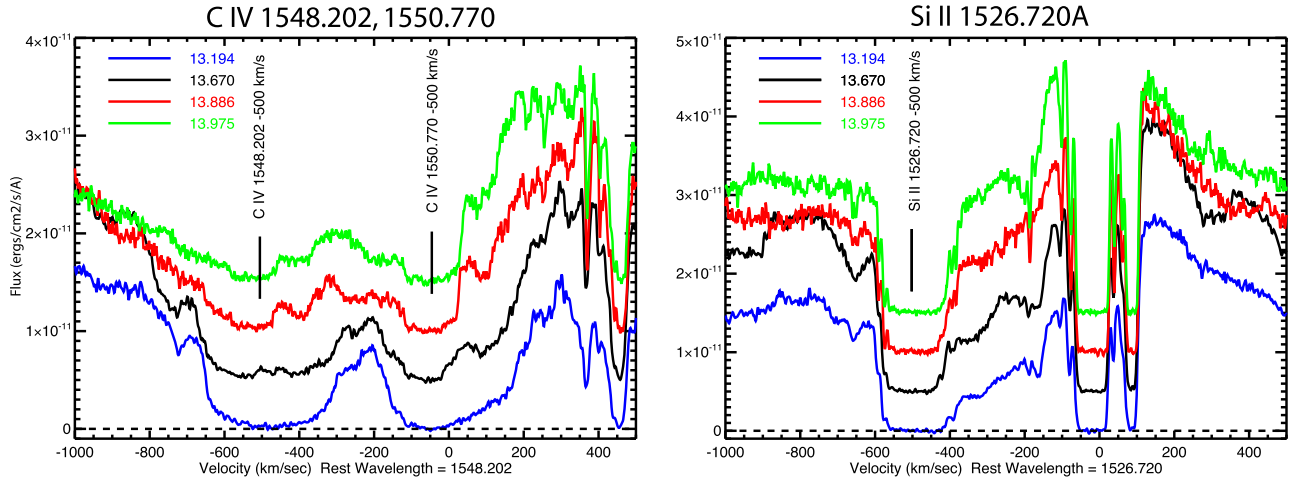


**Figure 22.** Evidence of the evolving distant WWC in our LOS across cycle 13 (from 2014.6 to 2020.1). The C IV absorptions centered at  $-500$  km s $^{-1}$  have evolved from a broad  $\approx 350$  km s $^{-1}$ -wide profile at  $\phi = 13.194$  to a substantially weaker  $\approx 150$  km s $^{-1}$ -wide profile at  $\phi = 13.975$ . Only a portion of the absorptions are black (total) at  $\phi = 13.194$ . The Si II  $\lambda$ 1527 (and Al II  $\lambda$ 1671, not shown) absorption is saturated from  $\approx -425$  to  $\approx -575$  km s $^{-1}$  with minimal changes across the entire cycle.

$\phi = 13.975$  and has disappeared by  $\phi = 14.022$ , which places an upper limit of 94 days on its appearance. This wing extends redward of  $-550$  to  $-1500$  km s $^{-1}$  and is present in most resonant line profiles (the N V velocity profile was too noisy to confirm the presence of the high-velocity wing across this interval).

By the early recovery to the high-ionization state, three spectra from early in cycles 11, 13, and 14 show strong absorptions at  $-500$  km s $^{-1}$ , but with very different widths (see Section 5.1 and Figure 6). Three-dimensional hydro models show that the downstream bow-shock structure can attain a terminal velocity up to  $V_\infty = 1000$  km s $^{-1}$  in the orbital plane. We measure  $V_\infty \approx 500$  km s $^{-1}$  in our LOS, which views the

orbital plane at  $49^\circ$ . The 3D hydro models of Madura et al. (2013) suggest that the half-opening angle of the wind-blown cavity is  $\approx 45^\circ$ , and the observational evidence is that we view the binary from within the cavity. Hence, the terminal velocity of the downstream shock should be somewhat greater than the primary wind terminal velocity accelerated somewhat by the secondary wind and radiation pressure.

The 3D hydro models show that a downstream bow shock persists for about 700 days, then breaks up (Madura et al. 2013, 2015). However, absorption at  $-500$  km s $^{-1}$  persists throughout the high-ionization state (Figures 10 through 12) and across the entirety of cycle 13 (Figure 22). The C IV  $\lambda\lambda$  1458,1551 absorptions approach saturation only near  $-500$  km s $^{-1}$  at

$\phi = 13.194$ , and become weaker with increasing orbital phase (Figure 22, left). However, the lower-ionization resonant lines, such as Si II (Figure 22, right), are saturated from  $-425$  to  $-575 \text{ km s}^{-1}$  and change minimally across cycle 13. Further modeling and observations are needed in order to determine if this phenomenon repeats and/or evolves.

Across periastron passage 11, because of the occulter, our LOS did not view much of the central core of  $\eta$  Car-A nor the effects of  $\eta$  Car-B on the WWC and the inner wind. As Gull et al. (2021) demonstrated, despite similar samplings of spectra in orbital phases, the borehole effect was not detectable in the STIS FUV across periastron passage 11, as the continuum component originating from the core of  $\eta$  Car-A was mostly blocked by the occulter. The occulter dissipated by cycle 14, allowing the borehole effect to be detected in the FUV. Likewise, the bulk of the changes in resonant lines across periastron passage 11 were limited to changes in the extended wind of  $\eta$  Car-A, but by periastron passage 14, modulation of the resonant lines by the WWC became much more obvious.

Our LOS is quite unique and has helped parse out much new information on changes in the previously ejected shells and in the WWC. Moreover, these observations, combined with our understanding of how the ejecta is expanding and dissipating with time, gives us pause to consider how  $\eta$  Car might appear at later times. Namely, when the Homunculus and Little Homunculus have dissipated in thousands of years, then observers will have a clear view of the interacting binary, if the binary members have not evolved to their final evolutionary stages. However, the Homunculus and the Little Homunculus continue to expand, and they will drop in surface brightness, eventually merging into the ISM.

## 7. Conclusions

The most significant finding of this study of FUV resonant lines is that we are now able to observe changes in the central core of the binary system and sample the effects of  $\eta$  Car-B and the WWC in our LOS. We summarize the main findings of this study below.

1. The FUV flux has increased tenfold over the past two decades.
  - (a) Most signatures of singly ionized metals at velocities  $-121$  to  $-168 \text{ km s}^{-1}$  have disappeared, indicating that the Little Homunculus has become more highly ionized in our line of sight.
  - (b)  $\sim 800$  absorption lines of  $\text{H}_2$  within the Homunculus have disappeared due to photodissociation through the Lyman bands.
  - (c) NaD absorption components at  $-146$  and  $-168 \text{ km s}^{-1}$  have weakened or disappeared in the high-ionization state, but briefly return during the low-ionization state associated with periastron passage (Pickett et al., in prep.)
  - (d) Absorption in the  $-100$  to  $-400 \text{ km s}^{-1}$  velocity range has decreased in C II, Si II, Al II, and Al III resonant lines, while absorption increased in Si IV.
2. The bore hole, created by the passage of  $\eta$  Car-B through the extended wind of  $\eta$  Car-A near periastron passage, became visible across periastron 14, but was not seen across periastron passage 11 (Gull et al. 2021) because the occulter preferentially blocked the continuum from

the core of  $\eta$  Car-A relative to emission from its extended wind.

3. The  $\text{H}\alpha$  emission equivalent width continues to decrease as the visible flux increases with the decreasing obscuration of the central core. However, slowing of the decline in  $\text{H}\alpha$  equivalent width (Damineli et al. 2021) may indicate that the rate of brightening is decreasing.
4. The high-velocity absorption component of C IV appears to have increased up to  $-2600 \text{ km s}^{-1}$  across the high state in cycle 13 relative to cycle 10 (Figure 10, left).
5. A transient absorption wing extending from  $-600 \text{ km s}^{-1}$  to  $-1500 \text{ km s}^{-1}$  appeared across periastron passage 14, but was not apparent across periastron passage 11. Its character is astonishingly similar across all resonant lines. We do not know if this is a one-time variation or a long-term trend, but suspect the latter. The most likely explanation is the trailing arm of the WWC passed through the LOS between the  $\eta$  Car-A continuum core in our LOS and our vantage point.
6. With the decreasing absorption of singly ionized metals in the multiple shells of the Little Homunculus, the profiles of Si II, Ni II, and Al II become more consistent with profiles generated by CMFGEN models of  $\eta$  Car-A.
7. The decrease in optical depth of the occulter allows us to use FUV resonant lines to provide a means to track the effects of the interacting winds and directly monitor any changes in flux and spectral features. The influence of the Homunculus absorbing systems in the LOS is decreasing and will continue to decrease.
8. We find no significant evidence for changes in the winds of the binary members.

Future studies, especially in the FUV, will become all the more important. We hope that HST/STIS access will continue through the next decade, as monitoring of changes of the FUV resonant absorptions before and during the next periastron passage in 2025 is now key to confirming the changes seen across periastron passage 14, assuming the changes in the winds are repeating.















The challenge posed by the FUV resonant lines must be met by modeling of the massive binary system and its wind interactions plus the changes in the multiple shells within the Homunculus and the Little Homunculus.

N.R. acknowledges funding from HST programs 15611 and 15992, which were accepted as supplementary observations associated with CHANDRA programs 20200564 and 21200197. M.F.C. is supported under the CRESST-II cooperative agreement #80GSFC17M0002 with the NASA/Goddard Space Flight Center. A.D. acknowledges FAPESP for support through process 2011/51680-6. A.J.F.M. is grateful for financial aid from NSERC (Canada). The work of F.N. is supported by NOIRLab, which is managed by the Association of Universities for Research in Astronomy (AURA) under a cooperative agreement with the National Science Foundation. C.M.P.R. acknowledges support from the National Science Foundation under grant No. AST-1747658. T.R.G. received no direct support for this study. We thank the referee for the careful and very prompt review of this lengthy study.

*Facility:* HST(STIS).

*Software:* CMFGEN (Hillier & Lanz 2001; Hillier 2011).

## ORCID iDs

Theodore R. Gull  <https://orcid.org/0000-0002-6851-5380>  
 D. John Hillier  <https://orcid.org/0000-0001-5094-8017>  
 Henrik Hartman  <https://orcid.org/0000-0001-9853-2555>  
 Michael F. Corcoran  <https://orcid.org/0000-0002-7762-3172>  
 Augusto Damineli  <https://orcid.org/0000-0002-7978-2994>  
 David Espinoza-Galeas  <https://orcid.org/0000-0003-2971-0439>  
 Kenji Hamaguchi  <https://orcid.org/0000-0001-7515-2779>  
 Felipe Navarete  <https://orcid.org/0000-0002-0284-0578>  
 Krister Nielsen  <https://orcid.org/0000-0003-2636-7663>  
 Thomas Madura  <https://orcid.org/0000-0001-7697-2955>  
 Anthony F. J. Moffat  <https://orcid.org/0000-0002-4333-9755>  
 Patrick Morris  <https://orcid.org/0000-0002-5186-4381>  
 Noel D. Richardson  <https://orcid.org/0000-0002-2806-9339>  
 Christopher M. P. Russell  <https://orcid.org/0000-0002-9213-0763>  
 Ian R. Stevens  <https://orcid.org/0000-0001-7673-4340>  
 Gerd Weigelt  <https://orcid.org/0000-0001-9754-2233>

## References

- Allen, D., & Hillier, J. 1991, *PASAu*, **9**, 120  
 Cantó, J., Raga, A. C., & Wilkin, F. P. 1996, *ApJ*, **469**, 729  
 Clementel, N., Madura, T. I., Kruip, C. J. H., Paardekooper, J.-P., & Gull, T. R. 2015, *MNRAS*, **447**, 2445  
 Corcoran, M. F. 2005, *AJ*, **129**, 2018  
 Corcoran, M. F., Liburd, J., Morris, D., et al. 2017, *ApJ*, **838**, 45  
 Dalgarno, A., & Stephens, T. L. 1970, *ApJL*, **160**, L107  
 Damineli, A. 1996, *ApJL*, **460**, L49  
 Damineli, A., Conti, P. S., & Lopes, D. F. 1997, *NewA*, **2**, 107  
 Damineli, A., Fernández-Lajús, E., Almeida, L. A., et al. 2019, *MNRAS*, **484**, 1325  
 Damineli, A., Hillier, D. J., Corcoran, M. F., et al. 2008, *MNRAS*, **386**, 2330  
 Damineli, A., Navarete, F., Hillier, D. J., et al. 2021, *MNRAS*, **505**, 963  
 Davidson, K., Ishibashi, K., Martin, J. C., & Humphreys, R. M. 2018, *ApJ*, **858**, 109  
 Espinoza Galeas, D. A. 2021, PhD thesis, The Catholic Univ. America  
 Falcke, H., Davidson, K., Hofmann, K.-H., & Weigelt, G. 1996, *A&A*, **306**, L17  
 Groh, J. H., Hillier, D. J., Madura, T. I., & Weigelt, G. 2012a, *MNRAS*, **423**, 3024  
 Groh, J. H., Madura, T. I., Hillier, D. J., Kruip, C. J. H., & Weigelt, G. 2012b, *ApJL*, **759**, L2  
 Groh, J. H., Nielsen, K. E., Damineli, A., et al. 2010, *A&A*, **517**, A9  
 Gull, T. R., Kober, G. V., & Nielsen, K. E. 2006, *ApJS*, **163**, 173  
 Gull, T. R., Madura, T. I., Teodoro, M., et al. 2016, *MNRAS*, **462**, 3196  
 Gull, T. R., Navarete, F., Corcoran, M. F., et al. 2021, *ApJ*, **923**, 102  
 Gull, T. R., Nielsen, K. E., Corcoran, M. F., et al. 2009, *MNRAS*, **396**, 1308  
 Gull, T. R., Vieira, G., Bruhweiler, F., et al. 2005, *ApJ*, **620**, 442  
 Hamaguchi, K., Corcoran, M. F., Gull, T., et al. 2007, *ApJ*, **663**, 522  
 Hartman, H., Damineli, A., Johansson, S., & Letokhov, V. S. 2005, *A&A*, **436**, 945  
 Hillier, D. J., & Allen, D. A. 1992, *A&A*, **262**, 153  
 Hillier, D. J., Davidson, K., Ishibashi, K., & Gull, T. 2001, *ApJ*, **553**, 837  
 Hillier, D. J., Gull, T., Nielsen, K., et al. 2006, *ApJ*, **642**, 1098  
 Hillier, D. J., & Lanz, T. 2001, in ASP Conf. Ser. 247, Spectroscopic Challenges of Photoionized Plasmas, ed. G. Ferland & D. W. Savin (San Francisco, CA: ASP), 343  
 Hillier, D. J., Lanz, T., Heap, S. R., et al. 2003, *ApJ*, **588**, 1039  
 Hillier, J. 2011, CMFGEN: Probing the Universe through Spectroscopy, Astrophysics Source Code Library, ascl:1109.020  
 Iping, R. C., Sonneborn, G., Gull, T. R., et al. 2005, *ApJ*, **633**, L37  
 Ishibashi, K., Corcoran, M. F., Davidson, K., et al. 1999, *ApJ*, **524**, 983  
 Johansson, S., & Letokhov, V. S. 2004a, *A&A*, **428**, 497  
 Johansson, S., & Letokhov, V. S. 2004b, *ApJ*, **48**, 399  
 Jura, M. 1974, *ApJ*, **191**, 375  
 Kiminki, M. M., Reiter, M., & Smith, N. 2016, *MNRAS*, **463**, 845  
 Madura, T. I. 2010, PhD thesis, Univ. Delaware  
 Madura, T. I., Clementel, N., Gull, T. R., Kruip, C. J. H., & Paardekooper, J.-P. 2015, *MNRAS*, **449**, 3780  
 Madura, T. I., & Groh, J. H. 2012, *ApJL*, **746**, L18  
 Madura, T. I., Gull, T. R., Okazaki, A. T., et al. 2013, *MNRAS*, **436**, 3820  
 Madura, T. I., Gull, T. R., Owocki, S. P., et al. 2012, *MNRAS*, **420**, 2064  
 Mehner, A., Davidson, K., Ferland, G. J., & Humphreys, R. M. 2010, *ApJ*, **710**, 729  
 Mehner, A., Davidson, K., Humphreys, R. M., et al. 2012, *ApJ*, **751**, 73  
 Mehner, A., Davidson, K., Humphreys, R. M., et al. 2015, *A&A*, **578**, A122  
 Morris, P. W., Gull, T. R., Hillier, D. J., et al. 2017, *ApJ*, **842**, 79  
 Nielsen, K. E., Corcoran, M. F., Gull, T. R., et al. 2007, *ApJ*, **660**, 669  
 Nielsen, K. E., Gull, T. R., & Vieira Kober, G. 2005, *ApJS*, **157**, 138  
 Pittard, J. M. 2007, *ApJL*, **660**, L141  
 Pittard, J. M., & Corcoran, M. F. 2002, *A&A*, **383**, 636  
 Richardson, N. D., Madura, T. I., St-Jean, L., et al. 2016, *MNRAS*, **461**, 2540  
 Shull, J. M., Darling, J., & Danforth, C. W. 2021, *ApJ*, **914**, 18  
 Smith, N., & Frew, D. J. 2011, *MNRAS*, **415**, 2009  
 Steffen, W., Teodoro, M., Madura, T. I., et al. 2014, *MNRAS*, **442**, 3316  
 Teodoro, M., Damineli, A., Heathcote, B., et al. 2016, *ApJ*, **819**, 131  
 The LIGO Scientific Collaborationthe Virgo Collaborationthe KAGRA Collaboration, et al. 2021, arXiv:2111.03634  
 Verner, E. M., Bruhweiler, F., & Gull, T. R. 2005, *ApJ*, **624**, 973  
 Walborn, N. R., Danks, A. C., Vieira, G., & Landsman, W. B. 2002, *ApJs*, **140**, 407  
 Weigelt, G., Albrecht, R., Barbieri, C., et al. 1995, *RMxAA*, **2**, 11  
 Weigelt, G., & Ebersberger, J. 1986, *A&A*, **163**, L5  
 Weigelt, G., Hofmann, K. H., Schertl, D., et al. 2021, *A&A*, **652**, A140  
 Werner, M. W. 1969, *ApJ*, **156**, 753  
 Zethson, T., Gull, T. R., Hartman, H., et al. 2001, *AJ*, **122**, 322  
 Zethson, T., Johansson, S., Hartman, H., & Gull, T. R. 2012, *A&A*, **540**, A133